Design, Implementation, and Evaluation of High-Efficiency High-Power Radio-Frequency Inductors

by

Roderick S. Bayliss III

S.B., Massachusetts Institute of Technology (2020)

Submitted to the Department of Electrical Engineering and Computer Science
in partial fulfillment of the requirements for the degree of

Master of Engineering in Electrical Engineering and Computer Science

at the

MASSACHUSETTS INSTITUTE OF TECHNOLOGY

February 2021

Author . . . .
Department of Electrical Engineering and Computer Science
January 15, 2021

Certified by. . . . .
David J. Perreault
Professor of Electrical Engineering and Computer Science
Thesis Supervisor

Accepted by . . . .
Katrina LaCurts
Chair, Master of Engineering Thesis Committee

Design, Implementation, and Evaluation of High-Efficiency High-Power Radio-Frequency Inductors

by

Roderick S. Bayliss III

Submitted to the Department of Electrical Engineering and Computer Science
on January 15, 2021, in partial fulfillment of the
requirements for the degree of
Master of Engineering in Electrical Engineering and Computer Science

Abstract

Radio-Frequency (RF) power inductors are critical to many application spaces such as communications, RF food processing, heating, and plasma generation for semiconductor processing. Inductors for high frequency and high power (e.g., tens of MHz and hundreds of watts and above) have traditionally been implemented as air-core solenoids to avoid high-frequency core loss. These designs have more turns than magnetic-core inductors and thus high copper loss; their high loss and large size are both major contributors to the overall system efficiency and size.

One contribution of this thesis is a magnetic-core inductor design approach that leverages NiZn ferrites with low loss at RF, distributed gaps and field balancing to achieve improved performance at tens of MHz and at hundreds of watts and above. This approach is demonstrated in a 13.56 MHz, 580 nH, 80 A_{pk} magnetic-core inductor design that achieves a quality factor of > 1100, a significant improvement over $Q{\sim}600$ achieved by conventional air-core inductors of similar volume and power rating.

This thesis additionally describes the difficulties in experimentally measuring inductor quality factors with very high current and very low loss at very high frequency. Several measurement techniques are proposed and evaluated to enable consistent measurement of inductor resistance at these operating points.

Finally, these design techniques are extended to an inductor design which achieves "self-shielding" in which the magnetic field generated by the element is wholly contained within the physical volume of the structure rather than extending into space as a conventional air-core inductor would. This development enables significant reductions of system enclosure volume and improvements in overall system efficiency.

Thesis Supervisor: David J. Perreault
Title: Professor of Electrical Engineering and Computer Science

Acknowledgments

Contents

List of Figures

List of Tables

Chapter 1

Introduction

Typically, magnetic components dominate the size and loss in power electronics. Due to magnetics fundamentals, these components perform worse as they're made smaller presenting an unfortunate trade-off between power handling capability and size [12]. Given the necessity of magnetics within many power electronics designs, designers are placed into a tough corner of fighting strict system requirements and physical limits.

An important subspace of the power field that is a focus in this research is radio frequency (RF) power electronics. RF is a very wide field encompassing historic challenges like telecommunications and emerging spaces like high power wireless power transfer and plasma etching. Magnetics designers within this space are again faced with physical limitations that severely hamper their ability to innovate and succeed. First, skin effect (a phenomenon that reduces the effective conduction area of a wire at AC) and proximity effect (in which fields generated by the inductor current impinge on other conductors inducing eddy currents and loss) become increasingly exacerbated as frequencies are pushed higher into the RF regime. Second, magnetic materials (often used to increase inductance or reduce fringing magnetic fields) often exhibit a loss characteristic that increases rapidly with frequency (i.e. $P_{\text{core}} \propto K f^{\alpha}$). Given these physical limitations (in addition to other limitations described later), designing efficient power inductors is a difficult task.

This thesis aims to develop techniques that enable vastly improved RF power inductors by leveraging advances in magnetic materials and innovative design method-

ologies.

Chapter 2 prevents the investigation and characterization of several magnetic materials. Core loss can be a significant limiter of a design's success especially at higher frequencies where traditional MnZn ferrites fall flat. Through characterization of new materials such as NiZn ferrites, more efficient, higher frequency magnetic elements can be produced, opening new design spaces (such as the use of magnetic materials in power magnetics at RF) that were previously closed.

Chapter 3 explores the design techniques and methodologies required to design high power, high frequency, magnetic-core inductors and presents a structure that utilizes these materials to achieve high performing inductors. Through a combination of magnetic field shaping and quasi-distributed gaps, conductor loss is significantly reduced compared to conventional air-core designs, yielding inductors with extremely high quality factors.

Chapter 4 presents an example RF inductor design utilizing the structure and design guidelines in chapter 3 yielding a modeled quality factor (Q) [1] of ≈1700 and a measured quality factor of >1100.

Chapter 5 presents the measurement techniques required to validate this quality factor. Accurately measuring the mΩ of resistance at a drive current of 80 A_pk and 13.56 MHz is no small task. The transformer-coupled resonant tank presented in this chapter achieves the fundamental requirements of both the production of 80 A_pk RF current and utilizing only simple voltage measurements.

Chapter 6 extends the design techniques developed in chapter 3 to a fully "self-shielded" structure in which no magnetic flux exists outside the physical volume of the structure. Using first principles loss and magnetics modeling and a brute force search, an optimized inductor design using this structure is presented and simulated.

---

[1]This thesis uses the following definition of inductor quality factor: $Q = \frac{\omega L}{R_\mathrm{ESR}}$, where R_ESR is the equivalent series resistance of the inductor at the frequency of interest. Note that this definition provides a value that is equal to 2π(peak energy stored)/(energy dissipated in a cycle) for a sinusoidal drive at the frequency of interest.

Chapter 2

Magnetics Materials Characterization

This chapter reviews a technique to accurately characterize the loss of magnetic materials in order to assess their potential for use in new power electronics' applications. It also describes a test fixture used for measuring loss, and presents representative data from these measurements. Magnetic materials such as ferrite or steel are beneficial in many designs as they typically provide non-zero relative permeability μ_r, enabling larger inductance per volume and greater design flexibility. However, these benefits do not come without the penalty of core loss. When magnetic materials are subjected to a time-varying magnetic flux, they generate heat. Today, this loss is very hard to model and must be empirically measured to predict a design's performance. This places designers in a conundrum as manufacturer's data at operating points of interest may not be reliable or even exist, and these losses are typically non-linear requiring accurate measurement at a large-signal drive level.

In order to accurately measure the core losses in various magnetic materials, the technique developed in [4] was used. Through this technique, schematically shown in Fig. 2-1, the device under test (DUT) inductor is resonated with a very low loss capacitor. By measuring the voltage across the capacitor (labeled v_{out}) and the voltage input to the tank (labeled v_{in}), the quality factor and resistance of the inductor (assuming the resistance of the capacitor and external resistances are negligible) can

be calculated as:

$$\frac{v_{\text{out}}}{v_{\text{in}}} = \frac{1}{1 - \omega^2 C_m L_m + (j\omega C_m)(R_{cu} + R_{\text{core}})} \tag{2.1}$$

$$\text{At resonance: } \left|\frac{v_{\text{out}}}{v_{\text{in}}}\right| = \frac{(\omega C_m)^{-1}}{R_{cu} + R_{\text{core}}} \tag{2.2}$$

$$R_{cu} + R_{\text{core}} = \frac{V_{\text{in,pk}}}{V_{\text{out,pk}}} \frac{1}{\omega C_m} \tag{2.3}$$

$$R_{\text{core}} = \frac{\omega L V_{\text{in,pk}}}{V_{\text{out,pk}}} - R_{cu} \tag{2.4}$$

If the resistance of the wire used to wind the inductor (R_{cu}) and the resistance of the capacitor (R_c) are small compared to the equivalent core loss resistance (R_{core}), the total resistance of the tank is approximately R_{core}.[1] A 50 Ω : 3 Ω transmission line transformer (PN AVTECH AVX-M4) was used to boost the low impedance of the series resonance to ≈ 50 Ω in order to extract pure, high power tones from the power amplifier. If the power amplifier is loaded with a resistance too far from 50 Ω, it is unable to produce the high-power, single frequency sinusoids requested from it. Finally, resonance is detected when the input and output voltage waveforms are 90° out of phase (with the input voltage leading). By adjusting the resonant capacitance and slightly deviating the frequency input to the tank from the nominal, desired frequency, resonance can be reached and core loss measurements obtained.

2.1 Performance Factor

In order to easily compare different materials, magnetic material performance factor was used as a figure of merit [8],[6],[11]. Conventional performance factor is defined by: $\mathcal{F} = \hat{B}f$ where f is the frequency of interest and $\hat{B}$ is the peak flux density that a material has some specified core loss density (in this case 500 mW/cm^3). Material performance factor can be directly related to the power handling capability of an

---

[1]If non-negligible, R_{cu} can be approximated and R_c measured under small-signal conditions or obtained from the manufacturer's datasheet.
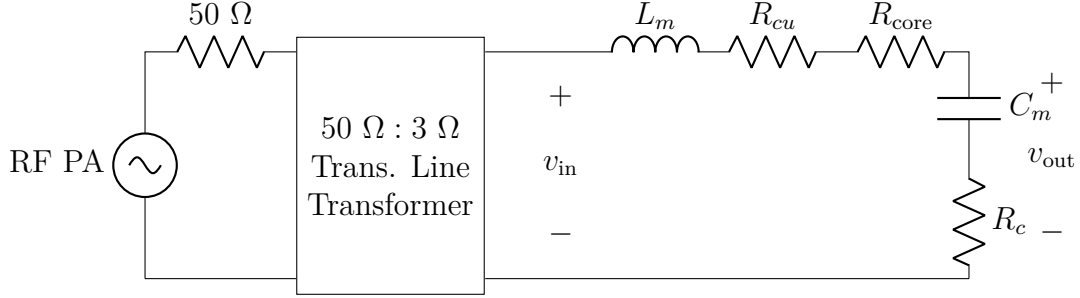
Figure 2-1: Magnetic materials loss measurement fixture schematic. The DUT inductor L_m is resonated with a low-loss capacitor C_m. By measuring the ratio of $v_{\text{out}} : v_{\text{in}}$, the quality factor of the resonant tank can be calculated and the core loss extracted. The transmission line transformer used was of type AVTECH AVX-M4.

inductor or transformer using that material at a given volume [9]. Materials that can handle higher flux densities at higher frequencies for constant power loss are thus "better" than other materials, allowing designers to quickly pick the best materials for their desired operation frequency. However, this performance factor metric does not account for variations in winding loss with frequency, and thus overestimates the achievable performance of a magnetic component at frequencies where one is skin-depth limited and cannot resolve this through use of litz wire or other methods. In order to capture the effect of skin effect limiting conduction area at higher frequencies, the modified performance factor $\mathcal{F}_{\frac{3}{4}} = \hat{B} f^{\frac{3}{4}}$ was introduced in [6], and is also utilized here.[2]

2.2   Test Fixture

The test fixture used to accurately characterize these magnetic materials is shown in Fig. 2-1. In order to generate sufficient core loss data, sweeps across frequency and drive level are used to generate graphs such as Fig. 2-2. Through interpolation (or extrapolation if necessary), the peak flux density at 500 mW/cm^3 of core loss can be extracted and the performance factor calculated. A MATLAB script (Appendix

---

[2]Resistance of a single layer winding R grows at $f^{1/2}$ due to skin depth reduction at higher frequencies. Additionally, the maximum winding current for a given power loss is proportional to $R^{-1/2}$, yielding the multiplication factor of $f^{1/4}$ and the modified performance factor $\mathcal{F}_{\frac{3}{4}} = \hat{B} f^{\frac{3}{4}}$.

Table 2.1: Magnetic Materials Component List

RF Power Amplifier	Amplifier Research 150A100B
Transmission Line Transformer	AVTECH AVX-M4
Capacitors	ATC 100B Series Capacitors
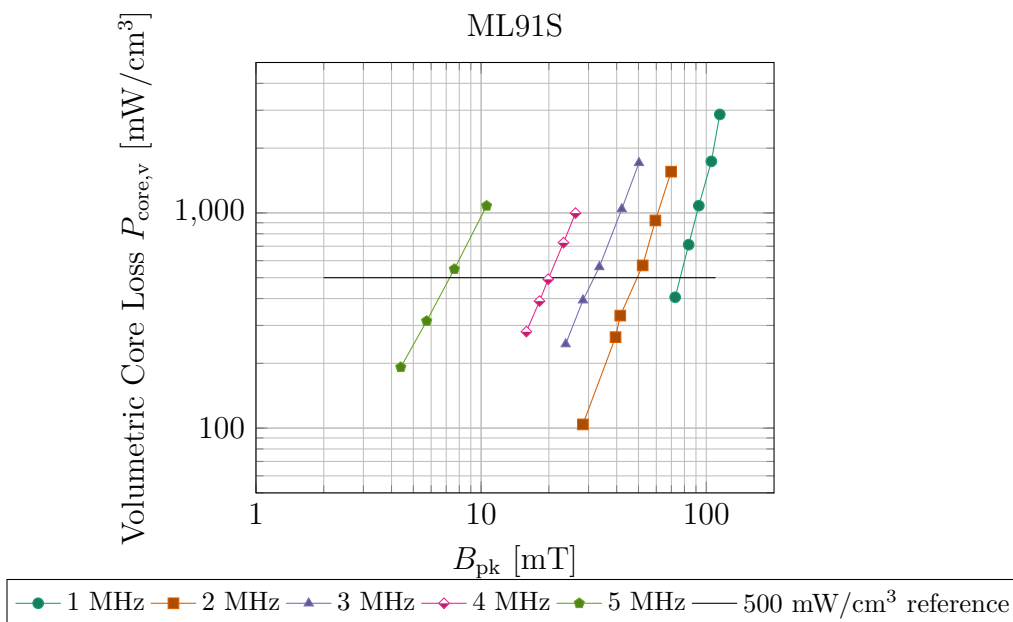
Figure 2-2: Measured core loss data for Hitachi Metals' ML91S ferrite material.

A) was developed to perform this interpolation and generate the performance factor curve vs. frequency for each material.

2.3   Results

2.3.1   Example Core Loss Data

Presented in Fig. 2-2 is example core loss data for Hitachi Metals' ML91S material gathered using the method described above. At higher frequencies, the core loss increases for a given magnetic flux density, indicated by the graphs moving "left" or "up" as the frequency is raised.

2.3.2 Performance Factor Graphs

Core loss data was gathered for various materials using the methods described above. Data entries labeled "Hanson" were obtained from the dataset in [6] while data entries labelled "Anna" were obtained from work done by a prior member in the group. The FerroxCube dataset is a compilation of the highest performing materials from the 2013 Soft Ferrites and Accessories Data Handbook, with most of these ferrites being MnZn. Fair-rite 67 performs extremely well in the 10-20 MHz range and was thus selected to be the material to be used in the inductor proposed in Chapter 4.
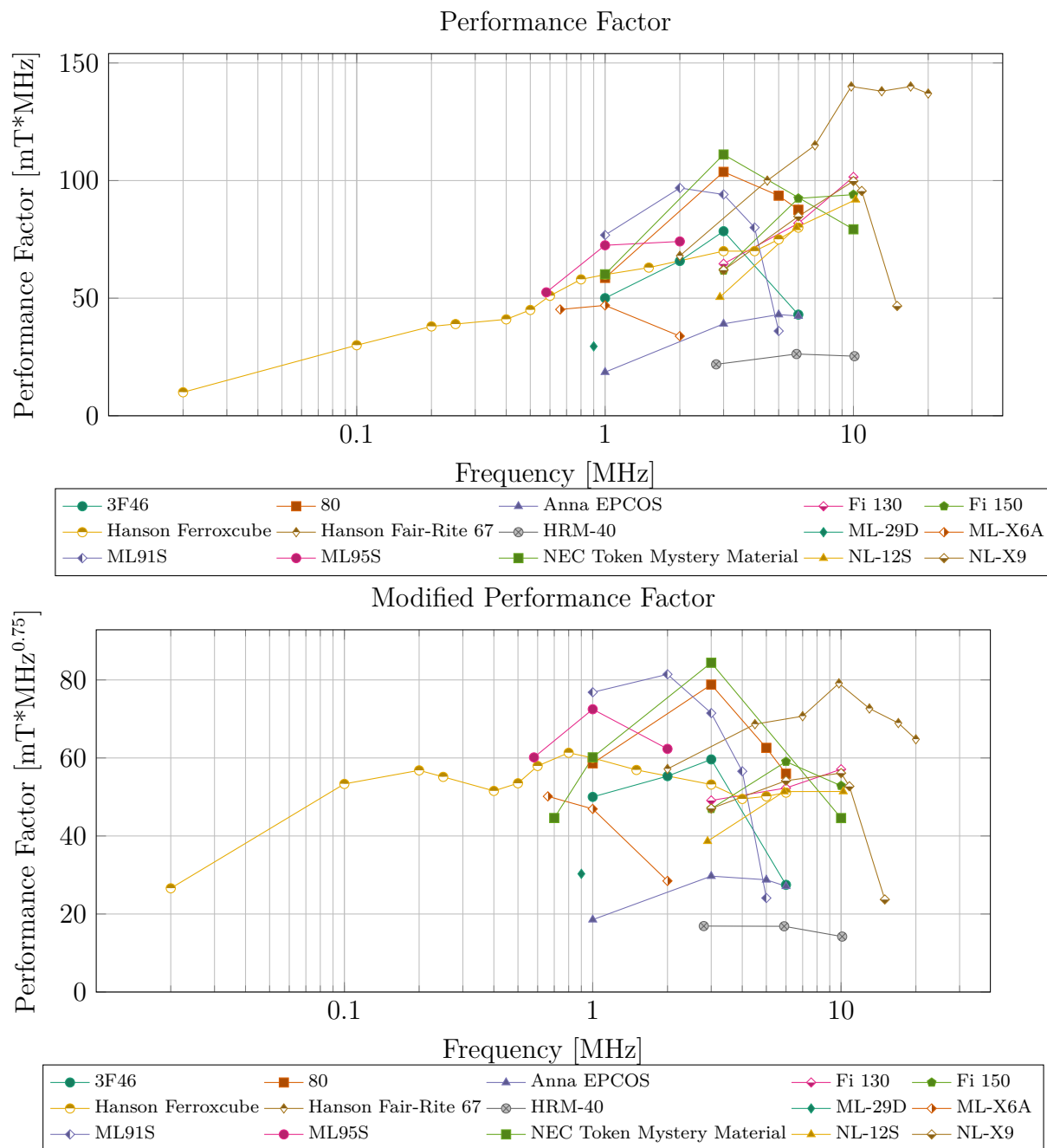
Figure 2-3: Compiled Performance Factor Graphs

Chapter 3

Proposed High Power RF Inductor Structure and Design

This chapter presents the design space and design methodology for a radio frequency (RF) high power inductor based on the use of a ferrite core material and a distributed gap.

3.1 Introduction

Magnetic components often dominate the size and loss of power electronic systems. These design challenges are significantly exacerbated for high-power systems at RF frequencies (e.g., the High-Frequency, or HF range of 3-30 MHz). First, conduction losses become challenging because skin effect greatly reduces the available effective conduction area of a wire at RF, while proximity effect prevents a designer from overcoming this by adding additional winding layers[1]. Second, traditional high-permeability power magnetic materials perform poorly in the HF range. A consequence of these considerations is that high-power RF inductors (such as for equipment operating at ISM frequencies of 13.56 MHz and 27.12 MHz) are typically designed as coreless solenoids (e.g., [3]) or occasionally as single-layer-wound toroids (e.g., [5]).

---

[1]Techniques such as litz wire become ineffective at these frequencies because of the lack of availability of litz comprising small enough wire strands.

Such inductor designs are physically large and often incur substantial loss. As RF systems are pushed towards higher efficiencies and power densities, new approaches towards RF inductor design are necessary.

One contribution of this thesis is a low-loss RF inductor design approach that leverages prior work [14], [15] by adapting it for higher frequencies, much higher power levels and larger sizes (e.g., kW power levels at tens of MHz). This design approach leverages high-performing low-permeability RF magnetic materials, and uses quasi-distributed gaps, a single-layer winding, and field balancing to mitigate conductor loss at RF. We find that, by scaling the approach in [14], [15], to much higher power and physical size, it is necessary to remove the permeable outer shell of the pot core and rely instead upon an uncontrolled flux return path through the surrounding air. This is a different and much more constrained design problem. We demonstrate this approach in the design of a 580 nH, 80 A_{pk}, 13.56 MHz inductor for RF power applications that achieves significant improvement in loss compared to conventional coreless designs at similar volumes.

3.2 RF Distributed Gap Dumbbell Inductor Design

3.2.1 Design Overview

The proposed inductor structure uses a dumbbell-shaped core geometry with quasi-distributed gaps in the center post (Fig. 3-1). The center post is constructed of alternating discs of ferrite and non-magnetic spacer material (e.g. plastic). Large ferrite end caps bookend a single-layer winding, which can be implemented with a copper tube. The end caps shape the flux path so that a reduced portion of the flux fringes axially out of the core (i.e. out of the "top" and "bottom" in Fig. 3-1).

(a) 3D Model   (b) Polar Cutaway
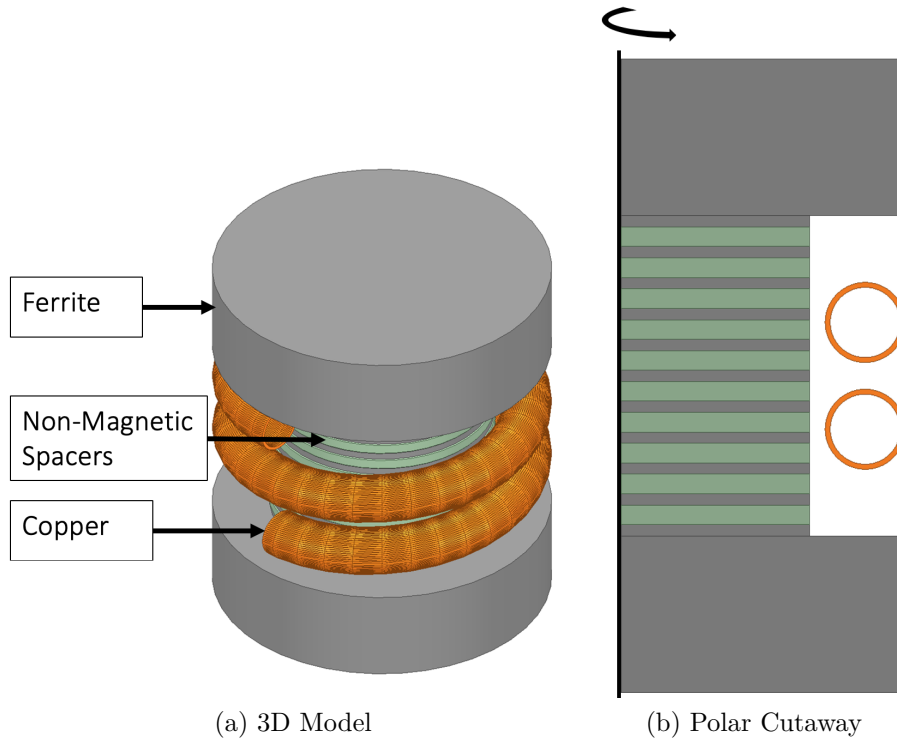
Figure 3-1: CAD model of the RF distributed gap inductor. Note that the polar cutaway of the structure doesn't account for the spiral nature of the coil.

3.2.2 Field Balancing and Quasi-Distributed Gaps for Improved Performance

In high-frequency inductors, current carrying is limited to conductor surfaces by skin effect, and current crowds towards conductor surfaces near larger magnetic fields. Field balancing, a design approach centered around the distribution of the magnetic fields around the conductors [14], [15], is one key technique used to dramatically increase the attainable performance in the proposed structure. Through this technique, the copper loss is reduced by maximizing the effective conduction area available in the wire to carry current by providing balanced fields on the wire surfaces.

In the structures in [14], [15] and in the proposed structure (Fig. 3-1), the magnetic field flowing up the center post and flowing back down the return path can be balanced to yield "double-sided conduction" in the wires, i.e. a skin of conduction close to the center post and a skin of conduction on the opposite side of the wires. In order to do
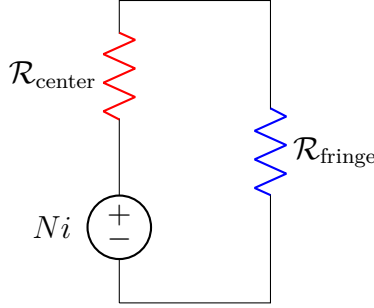
Figure 3-2: Magnetic circuit model for the "dumbbell" inductor. $\mathcal{R}_{\text{center}}$ represents the magnetic path within the barrel of the solenoid while $\mathcal{R}_{\text{fringe}}$ represents the magnetic path outside of the solenoid. The reluctance of the end caps is treated as negligible.

so, the reluctances in the magnetic circuit must be carefully designed. The magnetic circuit model for the proposed solenoid "dumbbell" inductor is shown in Fig. 3-2, in which the end cap reluctances are approximated as being negligible. $\mathcal{R}_{\text{center}}$ models the lumped reluctance provided by the distributed gap core in the "barrel" of the solenoid while $\mathcal{R}_{\text{fringe}}$ models the reluctance of the flux return path outside of the solenoid. If these reluctances are equal, they sustain the same MMF drop and hence the same $H = \frac{d(MMF)}{dl}$ on both sides of the wire, yielding two layers of conduction. An ANSYS finite element simulation [1] illustrates this effect in Fig. 3-3.
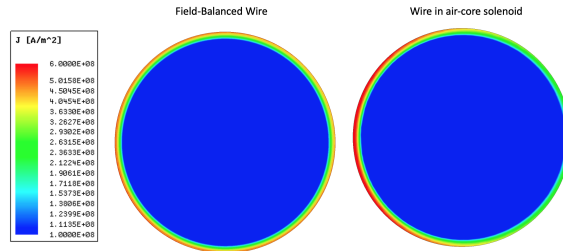
Figure 3-3: ANSYS FEA simulation illustrating the current crowding phenomenon. For the conductor on the right, the left hand side of the conductor is adjacent to the barrel of an air-core solenoid, a region with high reluctance and MMF drop compared to the outside of the solenoid. This MMF imbalance creates an asymmetry in the current distribution and increases loss. The conductor on the left is a miniaturized version of the wire in the proposed inductor and experiences much less current crowding due to the balanced nature of its surrounding magnetic fields. The example simulation runs at 13.56 MHz with an excitation current of 20 A_{pk}. The wires are 0.8 mm in diameter with the conductor on the right being part of a larger solenoid with an inner diameter of 6 mm.

The reluctance of the center post is set by using a quasi-distributed gap [7] as opposed to a single large gap. The quasi-distributed gap can greatly reduce eddy current losses caused by magnetic fields fringing from the gap(s) [7]. By increasing the number of gaps used in the structure, the strength of the fringing fields is reduced and the copper is able to be placed closer to the center of the structure. However, thin discs suffer from a lack of mechanical rigidity and increased complexity, forcing a design tradeoff.

The reluctance of the return path is set by the overall size of the structure ($\mathcal{R}_{\text{fringe}} \approx \frac{0.9}{\mu_0 \pi r_t}$ [2][13]). Here we see that the return-path reluctance decreases with the size of the structure, and therefore at a certain size and inductance target it is necessary to eliminate any other parallel return-path reluctance like the outer shell of a pot core. That is, to achieve perfect double sided conduction, $\mathcal{R}_{\text{fringe}} = \frac{N^2}{2L_{\text{desired}}}$. This requirement forces a strict relationship between the outer radius of the inductor r_t and the number of turns N where N may be similarly constricted to small values to reduce the copper loss incurred.

$$r_t = \frac{1.8 L_{\text{desired}}}{N^2 \mu_0 \pi} \tag{3.1}$$

A python script (Appendix B) was developed which outputted design geometries to achieve double-sided conduction. Given user input variables such as desired inductance, number of turns and gaps, the script returns the design geometries required the simulate and construct the inductor.

3.2.3 Optimum Aspect Ratio

Given the lack of first principles models of the losses within the structure, several manual sweeps are required to achieve an inductor which minimizes loss. One such design handle is the structure's aspect ratio (defined as total diameter to height). Smaller aspect ratios (i.e. taller, skinnier inductors) create a very long magnetic path

---

[2]Valid for structures where $h_t > \frac{2}{3} r_t$ where r_t and h_t are the outer radius and height of the inductor respectively
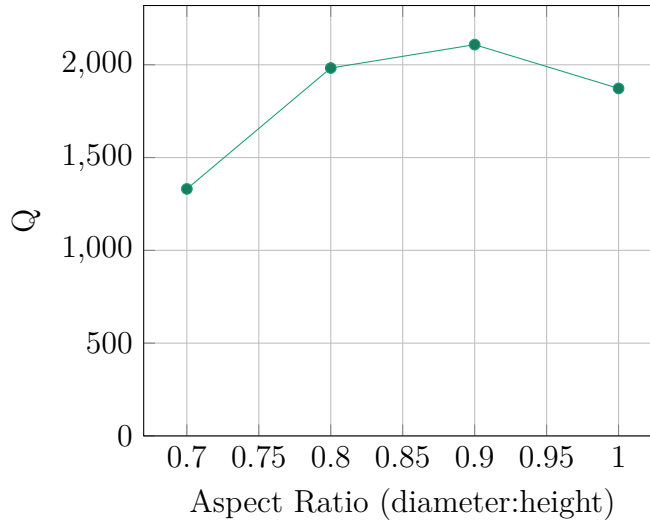
Figure 3-4: Quality factor vs. Aspect Ratio. Several inductor designs were simulated with inductance, number of turns, and number of gaps constrained. Here it was found that the optimal aspect ratio was 0.9. Note, since the outer radius of the inductor is constrained per Equation 3.1, the volume of the inductor is variable. However, larger volumes do not necessarily imply larger quality factors. The design point of $k = 0.9$ is also maximal on the Q vs. volume curve.

for flux to flow and provide very little core area. These two factors yield large core loss and create a lower bound on the aspect ratio. On the other end, large aspect ratios (short, pancake-like inductors) constrain the usable wire diameter, yielding large copper losses. In between these two extremes, a low-loss design can be achieved. An example of one such sweep is shown in 3-4. Here, the optimal aspect ratio was found to be 0.9.

3.2.4 End Cap Height

Although the reluctance of the end caps may be approximated as negligible compared to the reluctance of the distributed gaps, the loss within these elements may not be disregarded. Increasing the end cap height (thickness) helps to reduce the flux density and thus core loss within the pieces. However, the copper wire diameter must be reduced to accommodate the smaller window area, increasing copper loss

Given the difficulty of creating a model that fully captures this tradeoff, a manual sweep was done. With volume and r_t constrained, the end cap height was varied. The
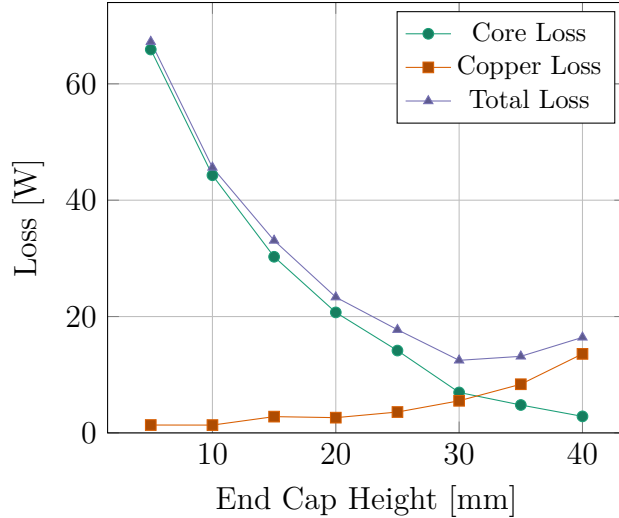
Figure 3-5: End Cap Height Sweep. After constraining the outer radius, k, inductance, number of turns, and number of gaps, the height of the end caps was varied. This design sweep illustrates the the tradeoff between core loss within the end caps and copper loss in the windings. The optimal loss balance to minimize total loss is found when core loss and copper loss are approximately equivalent.

results of this sweep are shown in Fig. 3-5. The volume of the inductor is constrained to be 1.16×10^{-3} m^3 and the total radius is 57 mm. The total loss of the inductor is minimized at end cap height = 30 mm. This design point strikes the balance of core loss in the end cap and copper loss in the windings.

3.2.5 Wire Size and Capacitance

Finally, selecting the optimal wire size presents the final manual search space required to generate an optimized low-loss inductor. The wire size presents a trade off of conduction loss and capacitance. It was found that the most dominant capacitance within the structure was the turn-to-turn capacitance of the copper coils. Thus by reducing the wire diameter and increasing the spacing of coil, the winding capacitance will be reduced at the expense of increased conduction loss. An example of one such sweep is shown in Fig. 3-6. The Q reported accounts for circulating currents created by the equivalent parallel capacitance of the structure. This estimated capacitance is generated by ANSYS Maxwell. However, Maxwell was found to seriously under-report the actual capacitance. All other variables except wire diameter were constrained.
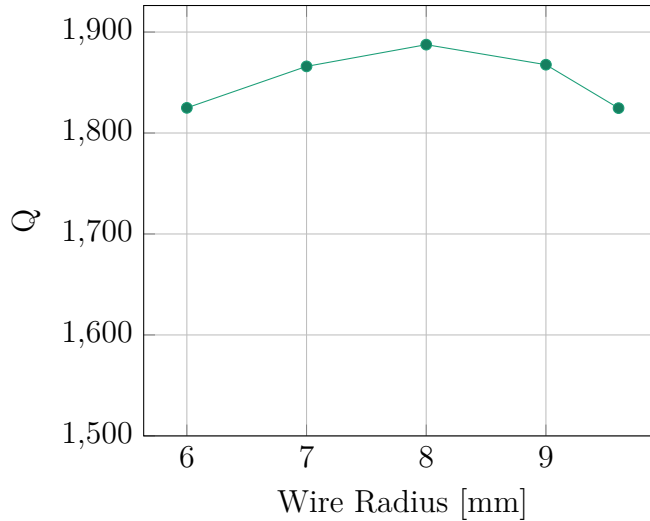
Figure 3-6: Wire Radius Sweep. By reducing the wire radius, the turn-to-turn capacitance is reduced, yielding smaller circulating currents due to this capacitance and increasing efficiency. However, this reduction in wire radius yields a smaller conduction area and thus increases conduction loss forcing a tradeoff. The quality factor presented here accounts for the turn-to-turn capacitance although this capacitance may be smaller than would be measured in real life as discussed in Section 5.5.

3.2.6 Loss Distribution

Generally in magnetics, designers are given the freedom to trade core and copper loss to minimize total loss through several design handles such as the number of turns. Typically, the overall loss of the element is minimized when the two losses are roughly equivalent; specifically the optimum ratio of core loss to copper loss is $\frac{2}{\beta}$, where β is the Steinmetz parameter for the magnetic material [9]. In this design space, however, it is desirable to penalize large core losses more than large copper losses. First, due to the high thermal conductivity of copper and the ability to remove heat through liquid cooling flowing through the center of the pipe, it is much easier to remove heat from the windings than the core pieces. Second, ferrites are prone to fracture under high thermal stress, and the core losses grow with temperature, yielding the potential for thermal runaway and designs that perform poorly under steady-state (rather than pulsed) operation.

3.3 Conclusion

This chapter presents a design approach for high-power inductors at RF frequencies (e.g., kW power scales at tens of MHz) that expands upon previously-developed techniques for high-frequency inductors at more modest power levels. The proposed design approach leverages low-permeability high-performing RF magnetic materials, single-layer windings, quasi-distributed gaps and field balancing to mitigate loss. The next chapter will provide detail about an example design.

Chapter 4

Example 580 nH Inductor Design and Construction

An example 580 nH inductor design using the proposed dumbbell structure (Fig. 3-1, repeated here as Fig. 4-1) was developed, simulated, constructed and experimentally tested. In simulation the design achieves a quality factor of ∼1700 at 13.56 MHz and 80 A_{pk}; as will be shown, the experimental quality factor has been difficult to accurately determine to date, but is at least 1100, and some measurements done suggest that it is approximately 1600. The inductor, whose structure is shown in Fig. 3-1, is approximately 100 mm in diameter and 110 mm in height. It uses Fair-Rite 67 as the core material and polypropylene for the plastic spacers for the distributed gap. Fair-Rite 67 was chosen as the core material as it was recently characterized [4], [6] to be high-performing in this frequency range and is a key enabler to the design's success. The winding is a custom wound 16 mm diameter copper tube with two full turns. A picture of the prototype inductor can be seen in Fig 5-3b.

4.1   Simulation Results

Presented in the following figures are simulation results from ANSYS Maxwell 2D Eddy Current solution solver. Simulations were run at an operating frequency of 13.56 MHz and peak current excitation of 80 A_{pk}. Core loss data for Fair-rite 67

(a) 3D Model   (b) Polar Cutaway
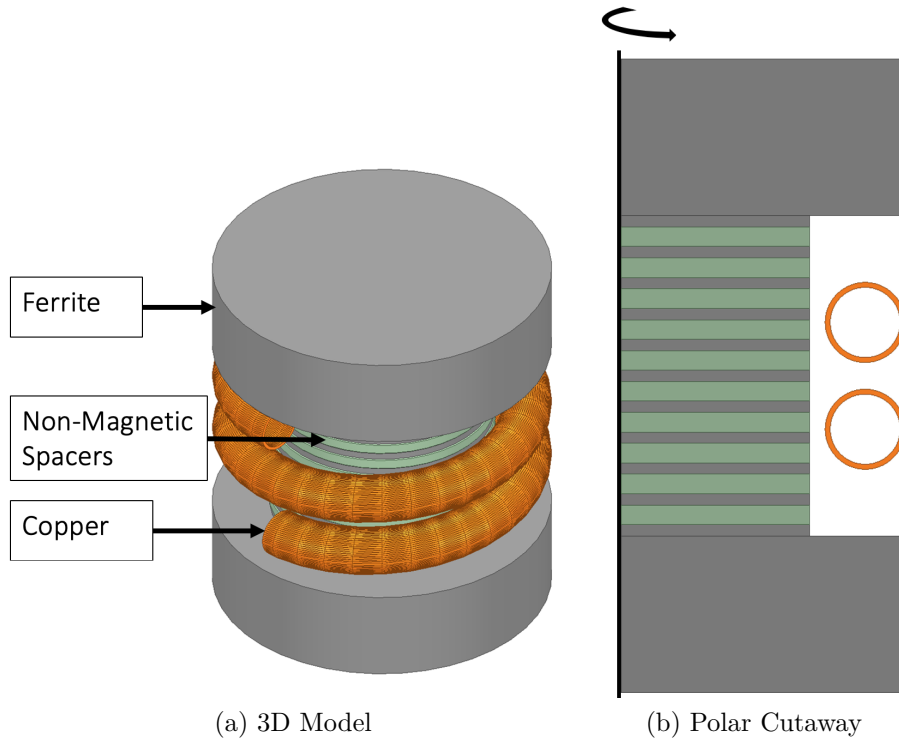
Figure 4-1: CAD model of the RF distributed gap inductor. Note that the polar cutaway of the structure doesn't account for the spiral nature of the coil.

Outer Radius	56.977 mm
End Cap Height	31.284 mm
Center-Post Radius	37.763 mm
Center-Post Ferrite Thickness	2.275 mm
Total Height	126.613 mm
Number of Gaps	10
Wire Diameter	16 mm
Number of Turns	2
Magnetic Core Material	Fair-rite 67
Plastic Spacer Material	Polypropylene

Table 4.1: Geometry of the Proposed Inductor
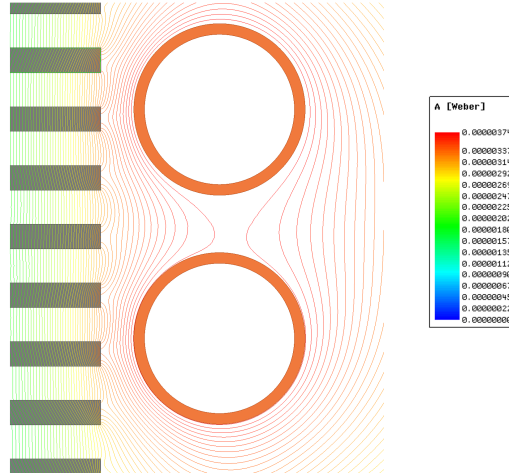
Figure 4-2: Magnetic Flux Lines of Proposed Inductor. The field lines on either side of the winding are well balanced yielding current sharing between the inner and outer sections of the winding, reducing copper loss. The simulation assumes a system temperature of 25°C with a fair-rite 67 core relative permeability of $\mu_r = 40$ and copper bulk conductivity $\sigma_{cu} = 58000000$ Siemens/m and copper relative permeability of 0.999991.

was gathered using the techniques described in Chapter 2 and input into the FEA solver[1]. Fig. 4-2 demonstrates the balanced nature of the magnetic fields on either side of the winding while Fig. 4-3 shows the current distribution due to these fields. At a system temperature of 25°C and copper bulk conductivity of $\sigma_{cu} = 58000000$ Siemens/m and copper relative permeability of 0.999991, the simulated copper loss is 43.434 W while the simulated core loss is 17.742 W yielding a total loss of 61.176 W. This coupled with the reported inductance of 500.56 nH yields a Q of 2120. If the equivalent parallel capacitance is assumed to be 30 pF, the simulated quality factor at 80 A_{pk} is 1697. In general, this capacitance is hard to predict, however given previous experimental results, this capacitance figure is reasonable for an inductor of this size

4.2   Inductor Construction

The copper windings are constructed of DHP C122 copper from `coppertubingsales.com`. The outer diameter of the winding is 16 mm and its wall thickness is 1 mm.

---

[1]Gathered P_{cv} v. $\hat{B}$ data was input into the solver. Maxwell then extracts the Steinmetz parameters from this dataset and calculates core loss based on these generated Steinmetz parameters.

(a) Inner edge of a turn   (b) Outer edge of a turn
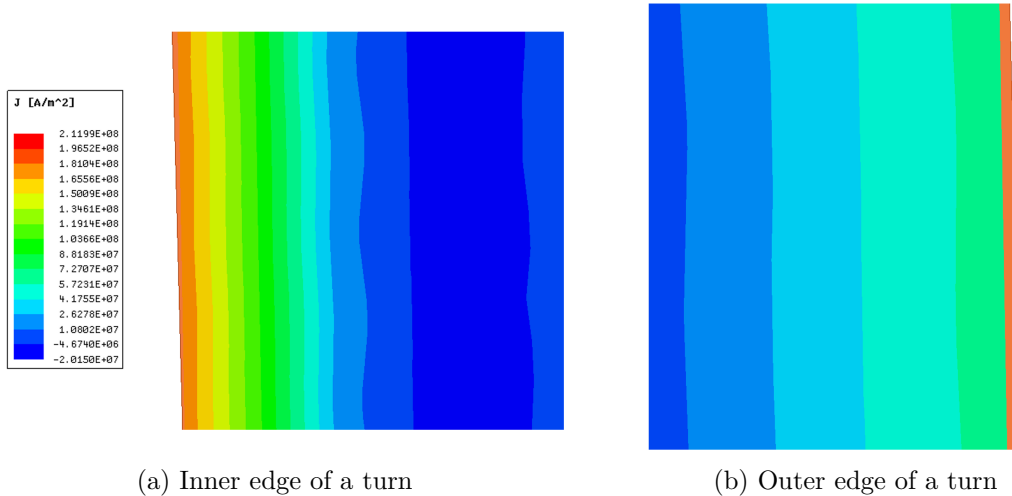
Figure 4-3: Current Distribution of Proposed Inductor. Both the inner and outer edges of the turns carry significant current, reducing copper loss. The simulation assumes a temperature of 25°C and a copper bulk conductivity of $\sigma_{cu} = 58000000$ Siemens/m and copper relative permeability of 0.999991.

The pitch of the coil is approximately 32 mm. The copper winding was formed from annealed copper tubing via a custom designed former fixture, shown in Fig. 4-4. After filling the annealed tubing with sand and sealing off either end, the tubing is inserted onto the fixture which is then affixed to a chuck. By rotating the chuck and bending the tubing, the copper coil can be formed.

Appendix F illustrates the CAD drawings used to manufacture the ferrite discs. Fair-rite both provided the magnetic material and manufacturing necessary to build the inductor. 1/8" thickness polypropylene plastic spacers were cut using a water jet in-house to form the distributed gap. The radius of these spacers was the same as the center-post ferrite discs. A circular cut-out in the center 2 mm in diameter was used in conjunction with a 1/16" diameter carbon fiber rod to ensure the concentricity of the discs.

In total, both end caps are made from two stacked 615.5 mil thick end cap pieces. The distributed gap is formed by alternating layers of 11 pieces of 89.6 mil thick ferrite and 10 pieces of 1/8" thick polypropylene (with ferrite forming the ends of the distributed gap stack).

36
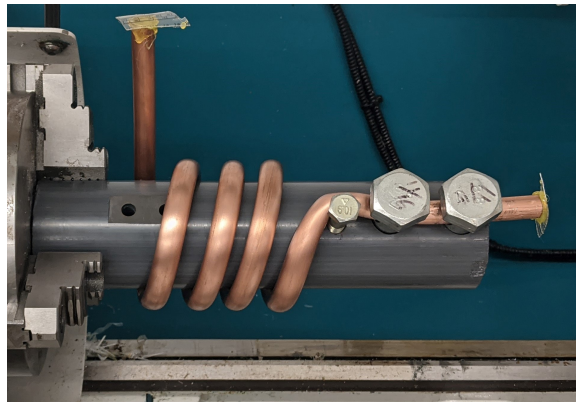
Figure 4-4: Copper Coil Former Fixture. The grey cylinder which the copper coil is wound around is a PVC rod 40 mm in diameter. Steel bolts are used to hold the right end of the coil in place as the cylinder is rotated and the coiled formed.

Chapter 5

Quality Factor Measurement Test Fixture

This chapter introduces the necessity and difficulties associated with characterizing the loss of high Q inductors at high currents and frequencies. It also demonstrates some useful techniques for overcoming these difficulties.

5.1 Motivation

An important aspect of developing high-quality-factor magnetic-core inductors is being able to accurately characterize their losses. Experimental validation of the quality factor at high power is challenging for many reasons. First, the losses in the ferrite are nonlinear, requiring the measurement setup to operate at the rated current of the inductor (in this case, 80 A_{pk}). Second, the very low losses in the inductor (equivalent series resistance on the order of tens of mΩ) are difficult to distinguish from other small losses in the test fixture. Finally, accurately measuring currents at RF is difficult; at minimum it requires expensive measurement hardware that may introduce additional loss in the system. Consequently it is best if the measurement technique relies only on the measurement of RF voltages or low-frequency (e.g., DC) voltages and currents.

Driving the measurement setup with high power sinusoids at HF (here, 13.56

MHz) is most easily accomplished using an RF amplifier. Typically, RF amplifiers are designed for 50 Ω systems. This has two main implications: first, to produce the required drive current (80 A_{pk}), the power amplifier would have to have a power rating of over 160 kW, a very large and expensive object. Second, although the power amplifier may be able to handle loads that are not exactly 50 Ω, the harmonic content begins to stray very far from the single-tone requested of the amplifier, creating measurement inaccuracies. These two issues necessitate a measurement system that presents 50 Ω to the input port and turns 50 Ω voltages and currents into low impedance voltages and currents (to obtain the higher drive current required).

The resonant tank method for measuring quality factor explored in Chapter 2 has the promising benefit of requiring only RF voltage measurements to extract the resistance of the inductor. A setup for this structure is illustrated in Fig. 5-2. To obtain the equivalent resistance R_L (and thus quality factor) of the inductor, first the capacitance or operating frequency must be tuned to resonance. Resonance can be found either when v_{input} and v_{reso} are 90° out of phase or when the maximal gain (i.e. $\frac{v_{\text{reso}}}{v_{\text{input}}}$ is maximized) is achieved. Assuming C_{reso} has internal resistance R_c and that there exists resistance external to the D.U.T., in series with the tank R_x:

$$v_{\text{reso}} = v_{\text{input}} \frac{(j\omega C_{\text{reso}})^{-1} + R_c}{j\omega L + R_L + R_x + R_c + (j\omega C_{\text{reso}})^{-1}} \tag{5.1}$$

$$\text{At resonance: } v_{\text{reso}} = v_{\text{input}} \frac{(j\omega C_{\text{reso}})^{-1} + R_c}{R_L + R_x + R_c} \tag{5.2}$$

$$R_L = \frac{v_{\text{input}}}{v_{\text{reso}}} \left| \frac{1}{j\omega C_{\text{reso}}} + R_c \right| - R_x - R_c \tag{5.3}$$

$$Q_L = \frac{\omega L}{R_L} \tag{5.4}$$

R_x can be estimated using finite element software upon the linkages connecting the D.U.T. to the capacitor and R_c was obtained using the vacuum capacitor's datasheet. R_x was estimated to be 4.8 mΩ and R_c was reported to be 4.14 mΩ.

A challenge with the resonant tank approach is that the resistance presented by the resonant tank at the operating point is far from 50 Ω, and requires higher current than a practical 50 Ω PA can provide, as described above. Consequently a substantial

degree of impedance transformation (or, equivalently, voltage and current transformation) is needed. However, by using a transformer to couple the PA (a 50 Ω system) to the resonant tank (a 10s of mΩ system), both requirements of input impedance matching and measurement ease can be achieved. This design - incorporating an $N:1$ transformer - is shown schematically in Fig. 5-2.

5.2   Transformer-Based Test Fixture Design

The test fixture design shown in Fig. 5-2, adapted for high power operation from the design in [4], allows us to measure the inductor quality factor at very high RF power levels and kV-scale RF voltages. This technique is extremely beneficial as it allows the user to extract the inductor's quality factor by measuring the ratio of two single-ended voltages' amplitudes. The D.U.T. is resonated with a low-loss vacuum capacitor and transformer-coupled to an RF power amplifier to drive pure-tone, high current sinusoids into the system. From measurements of the voltage across the transformer (v_{input}) and the resonant capacitor ($v_{\mathrm{reso,div}}$), one can calculate the resistance of the system and the inductor quality factor can be obtained. The injection transformer was implemented with 20 turns of triple insulated litz wire (Rubadue wire, 230 strands/44 AWG litz, PN TXXL230/44F3XX-2(MW80))) on a Fair-rite 67 toroid (PN 5967003801). The transformer's primary-referred leakage inductance was estimated to be 8.5 μH and magnetizing inductance 13.5 μH[1]. The copper tubing used to connect the inductor to the vacuum capacitor formed the single secondary turn.

Given the high quality resonance and large drive levels, a very large voltage is developed across the vacuum capacitor (≈ 4.7kV at the full drive current of 80 A_{pk}). In order to measure this RF voltage, a capacitor divider was used, shown schematically in Fig. 5-1. This voltage divider circuit is shown as the green PCB on the left in the Fig. 5-3a. The PCB contains a stack of 10, 5 pF Mica capacitors in series with a 22

---

[1]The transformer's leakage inductance was estimated using the leakage tuning capacitance C_{leak} described in Section 5.2.1. The transformer's magnetizing inductance was estimated using the manufacturer's A_L value with $N = 20$ with the leakage inductance subtracted from this value.
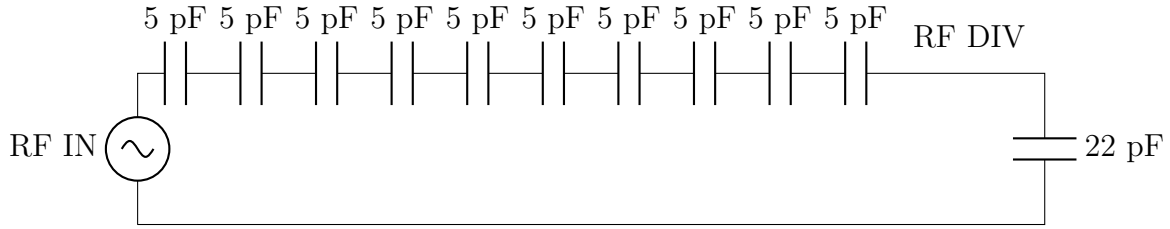
Figure 5-1: Capacitor Voltage Divider Schematic. The voltage across the 22 pF capacitor is 2.22 % times the "RF IN" input voltage. The capacitors used were all of type MC 1210 from Cornell Dubilier Electronics. Note, in reality there are parasitic capacitances that couple to the divided down node across the 22 pF capacitor, impacting the voltage division ratio.

pF Mica capacitor (Cornell Dubilier Electronics Type MC, 1210 size). Yielding an unloaded voltage division ratio of 2.22%. The schematic and layout for this PCB are provided in Appendix D. However, this division ratio is impacted by other external capacitances such as capacitance due to proximity to the conductive vacuum capacitor body or load capacitance in parallel with the 22 pF capacitor. The board is made of Rogers 4350B, low-loss PCB substrate and copper foil is used to connect the pads of the PCB with a screw on the capacitor plate. The vacuum capacitor (C_{reso} in Fig. 5-2) used was a Comet-PCT 50-500 pF variable vacuum capacitor with peak RF voltage capability of 9 kV (PN CVPO-500BC/15-BECA).

Fig. 5-3 illustrates both the CAD model of the test fixture shown schematically in Fig. 5-2 and the physical system. All copper elements were silver-plated with 0.5 mil of silver (plated by F. M. Callahan &: Son Inc. company of Malden, MA). The silver plating helps reduce the degradation of the copper surfaces over time as copper oxide is a semiconductor at room temperature while silver oxide is still considered a conductor. CAD drawings for the capacitor plates (1/4" thick 101 copper from McMaster-Carr) and other mechanical fixturing details are provided in Appendix G. The connecting tubing is formed from 16 mm outer diameter, 1 mm wall thickness DHP C122 copper from `coppertubingsales.com`. Solder-connect elbow and reducer fittings from McMaster-Carr were used to connect the capacitor plates to the inductor.
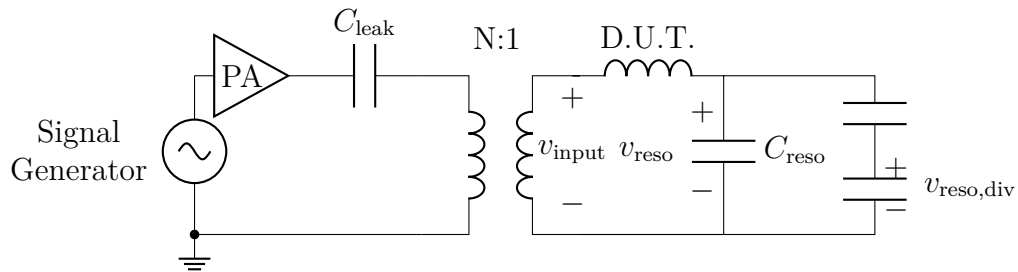
Figure 5-2: Simplified Inductor Quality Factor Measurement Fixture Schematic. The D.U.T. inductor is resonated with a low-loss capacitor. The series resonant tank is transformer coupled to a power amplifier in order to present an impedance close to 50 Ω to the PA and extract a pure tone. The large resonant node voltage is divided down and measured using a capacitor divider shown in the right of this figure. C_{leak} resonates out the transformer's leakage inductance as discussed in 5.2.1. Note the transformer schematically shown here is not ideal and includes parasitics such as leakage and magnetizing inductance and winding and core resistances.

(a) CAD Model

(b) Setup
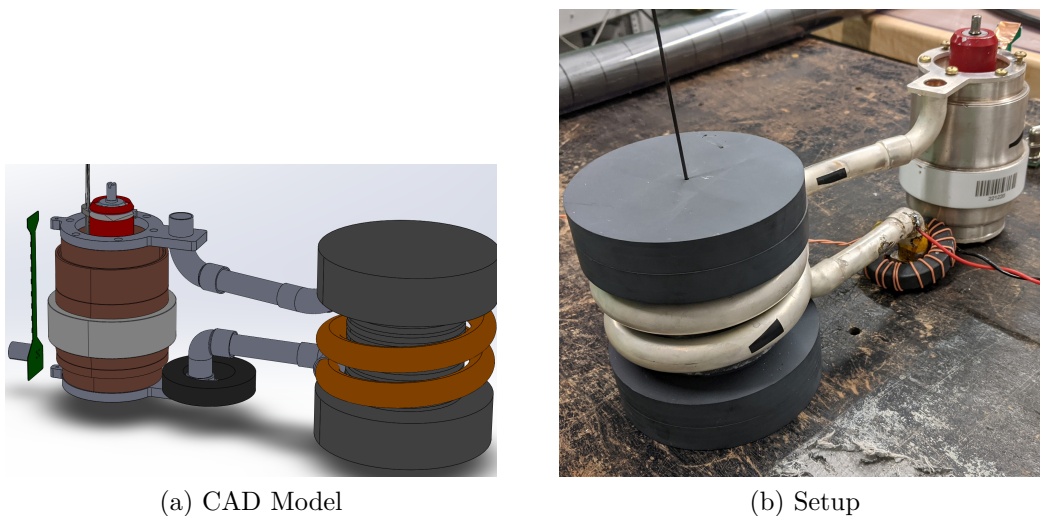
Figure 5-3: Inductor quality factor validation test fixture with prototype inductor.

5.2.1 Tuning Requirements

Due to the nature of operating at RF, there are many parasitics in the system that either need to be calibrated out or otherwise avoided. Given the nature of the single-frequency, sinusoidal operation of the system, resonance is a very powerful tool able to turn pesky parasitics into shorts or opens. One such parasitic is the leakage inductance of the transformer. It causes a decrease in the series resonant frequency of the tank when viewed at the power amplifier port of the transformer rather than looking directly into the resonant tank of interest. This is undesirable as the impedance of the tank (looking into the PA's transformer port) at the maximal gain frequency may have a significant inductive component, degrading the input match and the quality of sinusoids produced by the power amplifier. However, this nonideality can be resolved by the insertion of a capacitor in series with the transformer leads (C_{leak} in Fig. 5-2). By tuning this capacitor to resonate with the transformer's leakage inductance at the frequency of interest (the maximal gain frequency of the resonant tank), the leakage inductance's adverse impact can be negated. An impedance analyzer (Agilent 4395A) was used to extract the impedance vs. frequency looking into the transformer port seen by the PA and the capacitance was tuned such that the frequency of minimum reflection (i.e. minimum $|\Gamma_{\text{L}}|$) coincided with the maximal gain frequency of the tank. The capacitors used were ATC 100B placed on a PCB made of Rogers 4350B substrate[2]. Finally, the reactive voltage these capacitors sustain may be larger than the voltage rating of a single, reasonably sized capacitor, requiring the use of a series stack of capacitors.

Lastly, the turns ratio of the transformer must be tuned to obtain a series resonant impedance as close to 50 Ω as possible. However, the turns ratio isn't as simple as 50 $\Omega = N^2$(resonant tank impedance). This turns ratio must be determined experimentally. In general, the minimum of the input impedance $|Z_{\text{in}}|$ is not the series resonant impedance, illustrated in Fig. 5-4. Because of this, the number of

---

[2]The PCB used to mount these capacitors was the same as the capacitor divider PCB (Appendix D), with material manually removed such that only the top 7 capacitor pads and input pad was present.
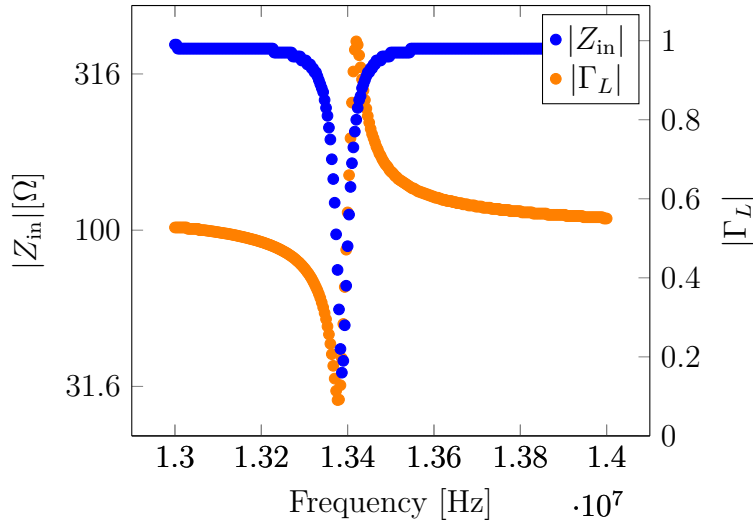
Figure 5-4: Example Input Impedance. Note that the frequency where $|Z_{in}|$ is minimal is not the same as the frequency where $|\Gamma_L|$ is minimal, where resonance actually occurs. Data gathered using an Agilent 4395A.

turns should be tuned such that the impedance at the frequency where $|\Gamma_L|$ is minimal, not the frequency where $|Z_{in}|$ is minimal, is as close to 50 Ω as possible. This effect is due to the long transmission line that connects the PA/impedance analyzer to the tank and primary capacitance on the transformer. In general, the order of operations for parasitic tuning is first choosing the correct number of primary turns to yield the correct resonant impedance then adjusting the leakage capacitance such that the minimum reflection frequency and maximal gain frequency of the tank are coincident.

A full schematic illustrating these parasitics is provided in Fig. 5-5. A photo illustrating the PCB which contained C_{leak} is provided in Fig. 5-6.

5.2.2 Transformer Power Handling

To process the full load current required, the injection transformer is placed under considerable stress. Its large turns ratio and the 100s of watts that flow through this device can yield considerable core and copper loss. Thus, design of the transformer must be executed with this limitation in mind. This is especially problematic if the system is operated off resonance as the large reactive voltages generated by the resonant tank appear across the magnetizing inductance of the transformer, inducing
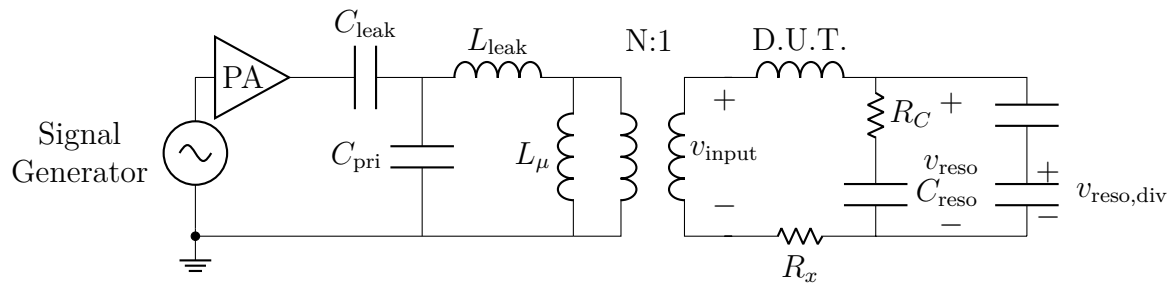
Figure 5-5: Inductor Quality Factor Measurement Fixture Schematic Including Parasitics. C_{pri} models the equivalent primary capacitance of the transformer. Values for the transformer parasitics are given in section 5.2 while values for the parasitic resistances of the secondary tank are given in section 5.1. Resistors which model the transformer's winding and core loss are not included.

Figure 5-6: Birds' Eye View of Transformer Coupled Resonant Tank Test Fixture. The green PCB in the bottom left of the photo houses C_{leak}. By manually tuning this capacitance, the impact of the transformer's primary-referred leakage inductance can be nulled.

considerable core loss.

5.3   Local Rectification/RF Detection

5.3.1   Earth Abnormalities

For safety reasons, lab equipment, such as amplifiers and oscilloscopes, reference their grounds to the mains' earth connection. This is incredibly important as if there is a failure such that the chassis of the case or ground terminal is live with mains voltage, a breaker can trip and users are protected. This safety feature however creates complications in that the earth connection provides a path for common mode currents to flow. Both the power amplifier and oscilloscopes used in this setup connected the negative terminal of the output and probe input, respectively, to earth (illustrated in Fig. 5-8). These two connections to earth were shorted together through the lab bench.

At low frequencies of operation, these two systems are isolated by action of the transformer. However, due to parasitic capacitive coupling between the transformer windings, at high frequencies this isolation barrier breaks down and currents are able to capacitively couple across the transformer. This isolation-jump coupled with the earth connection present on the oscilloscope provides a potential path for currents to flow from the PA's (earthed) negative terminal, capacitively couple to the secondary and flow through the scope's earth connection back to the PA. Additionally, conventional differential probes are not an adequate solution. Low voltage differential probes that may have enough capacitive isolation from differential input to ground often cannot withstand the voltage required and high voltage differential probes typically have too much capacitance from differential input to ground to isolate the oscilloscope's earth from the measurement system. Potentially, optically isolated differential probes possess both the isolation and voltage headroom required. However, at the time of writing, the cost of this solution was prohibitive.

Several tests were instituted to prove the presence of common mode currents

Figure 5-7: "Ground to Ground" Probe. The voltage measured on the oscilloscope is indicative of common mode ground currents.

causing measurement inaccuracies. The most significant being the use of a "ground to ground" probe where a 3rd probe was connected to the tank with both the ground and signal lead connected to the same point on the bottom capacitor plate, shown in Fig. 5-7. Normally this configuration is viewed as a sort of magnetic field detector as the voltage across the loop is proportional with the time derivative of flux passing through the loop formed by the probe ground lead. However, this configuration is also able to detect differences in ground potentials which could be created by common mode currents flowing into the scope and into the mains earth connection. When connected to the tank and scope, this "ground to ground" probe measured a voltage of 3.5 Vpp. This voltage was significantly higher than any voltage measured near the inductor where the magnetic field strength would be highest, indicating that the voltage is primarily due to ground currents rather than magnetic fields. Additionally, the probe caused a peculiar reduction in output voltage when plugged into the scope. If the probe was unplugged from the scope (but still connected to the tank), the output voltage was 17.05 Vpp however on plugging the probe into the scope, the output voltage was reduced to 3.5 Vpp. This is likely due a combination of a shift in tank resonant frequency and ground currents.
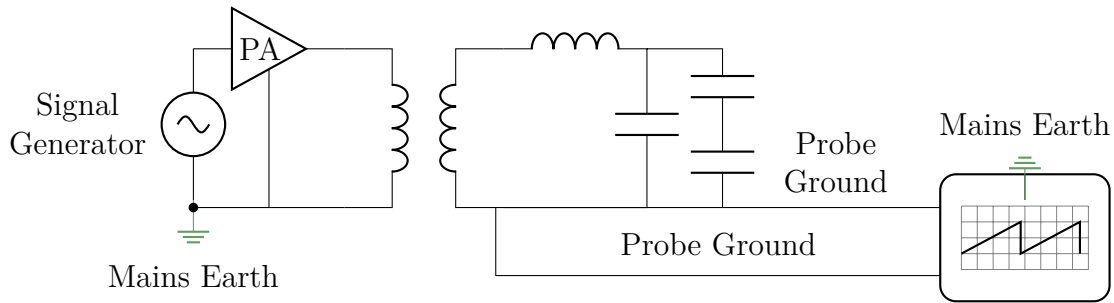
Figure 5-8: Schematic illustrating earth connections
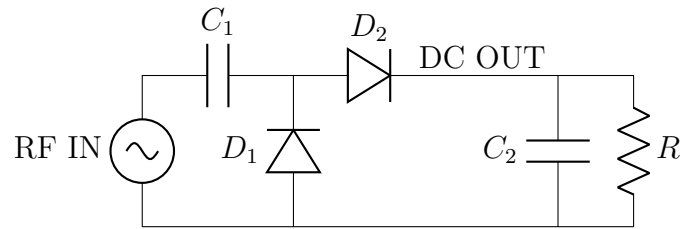
Figure 5-9: Voltage Doubler RF Probe Schematic. The parts list for the PCB which implements this schematic is given in Table 5.1. Appendix E includes the schematic and layout design files.

5.3.2 Voltage Doubler RF Probe

In order to circumvent the issues introduced by passing an earthed RF connection from the scope to the resonant tank, an RF detection approach based on local rectification of the sensed AC voltage was used [2]. Per Equation 2.3, only the amplitudes of the RF waveforms are required to calculate the quality factor of the inductor as long as the harmonic content is low and Q is calculated at the maximal gain point of the tank.

By rectifying the RF voltage, producing a DC voltage proportional to the peak of the RF voltage applied to the rectifier, a DC signal proportional to the RF voltage can be synthesized, and read by an isolated multimeter, eliminating the issue introduced by the earth connection in the oscilloscope. Essentially, this technique uses diodes to convert the signal of interest from the RF frequency down to DC where it can be read without interference, and where any broader EMI generated by the setup becomes unimportant. To implement the probe detector, the voltage doubler rectifier topology was used (shown schematically in Fig. 5-9). This topology presents a high impedance

49
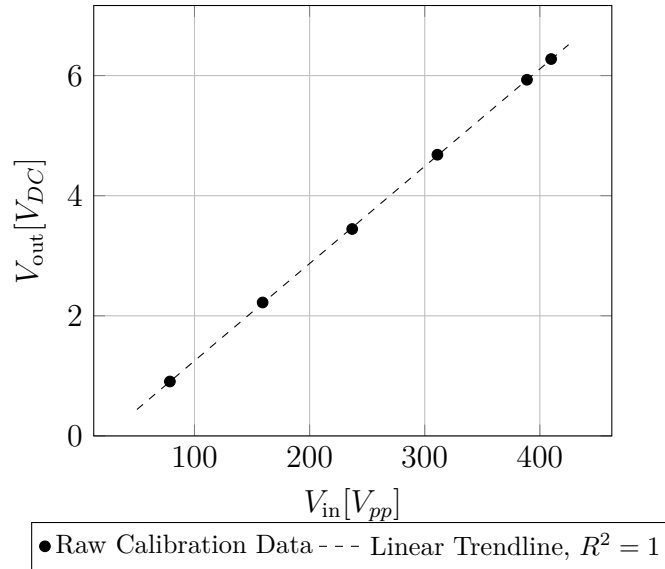
Figure 5-10: Example Voltage Doubler RF Probe and Capacitor Divider Calibration. A large RF voltage is applied to a 50 Ω resistor. The vacuum capacitor (used in the resonant tank) and capacitor divider are placed in parallel with this resistor. Graphed is the output voltage of the voltage doubler vs. the RF voltage applied across the 50 Ω resistor.

to the tank at DC, reducing the parasitic load presented by the doubler, and does not draw any dc current from the capacitor divider as some single-diode detectors might do.

Calibration of the voltage doubler RF probe is especially important as the non-linear capacitances of the diodes (mainly functions of the DC voltage on the output of the doubler) and the positioning of the doubler, which introduce variable parasitic capacitances, vary the transformation ratio of the capacitor divider on the resonant node of the tank. An example of a calibration dataset (calibrating both the capacitor divider and voltage doubler) is shown in Fig. 5-10. An image of the data collection setup is shown in Fig. 5-11 and is schematically shown in Fig. 5-12. Low capacitance Schottky diodes were used due to their short recovery times and reduced impact on the transfer function of the capacitor divider. A full description of the RF probe design, including layout, connectors, etc., can be found in Appendix E.
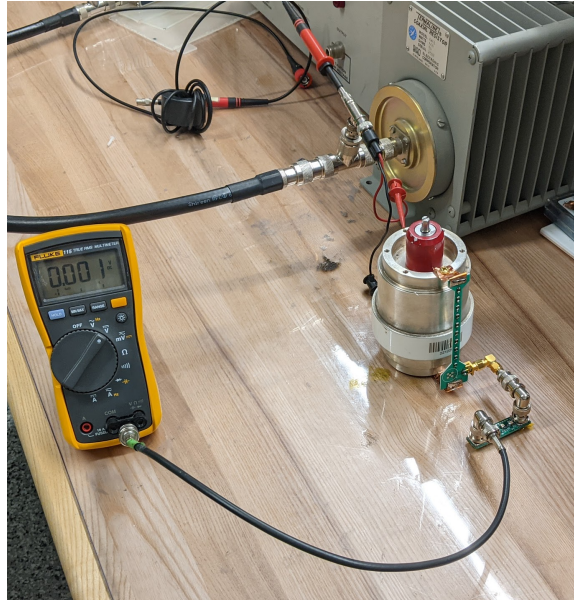
Figure 5-11: Voltage Doubler RF Probe Calibration Fixture. an N connector Tee joins the RF input, the 50 Ω resistor, and a BNC Tee. A Lecroy PPE 4 kV probe connected to the oscilloscope and a BNC to test lead clip are connected to this BNC Tee. The test lead clips are attached to the vacuum capacitor to which the capacitor divider is connected. Finally, the RF probe is connected to the output of this capacitor divider.
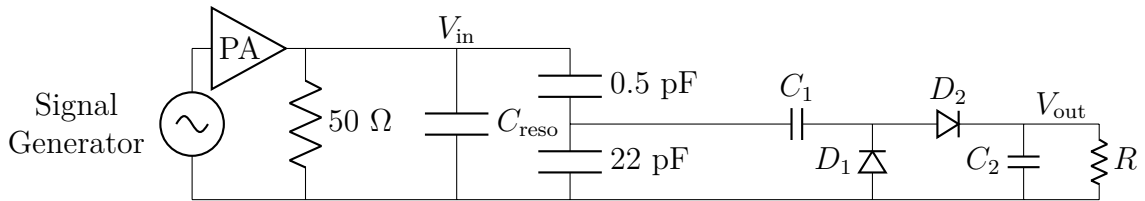
Figure 5-12: Voltage Doubler RF Probe Calibration Fixture Schematic

C_1	ATC 100B Series 120 pF
C_2	ATC 100B Series 1 nF
D_1 & D_2	Macom MA4E1340B1 70 V Schottky diodes
R	0805 2 MΩ||Multimeter Input Resistance (10 MΩ)

Table 5.1: Voltage Doubler Part Numbers

5.4 Air-Core Comparison

To validate the measurement methods presented above, an air-core inductor of similar inductance as the proposed inductor was constructed. Given the lack of non-linear loss characteristics, the inductor's quality factor can be measured at small signal with an impedance analyzer and compared with large signal measurements made using the transformer-coupled resonant tank. The solenoid was constructed of 3 turns of 16 mm copper (wall thickness of 1 mm). The inner radius of the solenoid was 40 mm and its pitch was 32 mm. Its inductance was measured as 532.03 nH at 13.56 MHz. This inductor was also used as a basis for comparison with the cored prototype inductor.

Given the inductance and resistance of the solenoid, it is almost impossible for an impedance analyzer to separate the mΩs of inductor parasitic resistance from the 10s of Ω reactance when looking into the inductor directly. To solve this issue, the inductor is resonated with a vacuum capacitor at the frequency of interest. The resonance nulls the reactive component of the series RLC circuit and the impedance analyzer is able to extract the resistance. Using this method, the small signal quality factor obtained was 1096.[3] The minimum impedance of this series resonant tank was found to be 43.97 mΩ. After subtracting out DC resistance measurements of the connecting leads (estimated as 1.52 mΩ) and the capacitor ESR (approximately 4.02 mΩ), the inductor resistance was found to be 38.43 mΩ.

The large signal quality factor obtained by measuring a coreless inductor with the proposed resonant measurement setup was a Q of 1192 at 13.435 MHz and $I_{\mathrm{pk}} = 19.47$ A, corresponding to an estimated ESR of 37.7 mΩ. This result is very close to that found via the small-signal measurement (considering the fixturing differences between the impedance analyzer measurement and the high-power test stand), validating the measurement apparatus.

---

[3]The inductor used in this small signal Q measurement is slightly different from the large signal inductor and has an inductance of 508 nH. These differences are attributed to manufacturing differences between the two coils.

5.4.1 Inductor Effective Volume

To create a fair comparison between this air-core inductor and the proposed inductor, the "effective volume" of both structures were used. This volume was defined by the minimum cylindrical volume surrounding the inductor such that the quality factor and inductance when placed within this metal box degraded by no less than 5%. This box volume is indicative of the region of high-strength magnetic fields. The inner radius of the metal box was 257.77 mm with an inner height of 186.613 mm, yielding a total volume of 38.95×10^{-3} m^3. This constraint yielded the solenoid dimensions given above.

5.4.2 Q Spoiling

In order to provide a check on the validity of measurements made using the transformer coupled resonant tank and voltage doubler, an intentional, lossy element was added to the circuit. By inserting a 0.5" diameter steel rod into the "barrel" of the air-core solenoid, the quality factor measured with the experimental system dropped from 1192 to 375, validating that the measurement apparatus is able to detect the introduction of new losses into the system.

5.5 Results

The inductor quality factor was characterized using two methods. First one where the RF waveforms v_{input} and $v_{\mathrm{reso,div}}$ were measured directly by an oscilloscope and the second using the voltage doubler RF probe method described previously.

The simulated and measured quality factor of the inductor are plotted in Fig. 5-13 as a function of peak current at 13.56 MHz. These measurements were obtained using two single-ended probes and an oscilloscope. At the highest current point of 82.5 A_{pk}, a Q of 1650 was achieved, nearly a factor of 3 better than a similarly-sized air-core inductor at similar operating conditions (709 nH, 77.5 A_{pk}, 10.9 MHz, $Q = \sim\!600$) [3]. These results also match up well with the simulated Q of approximately 1700.
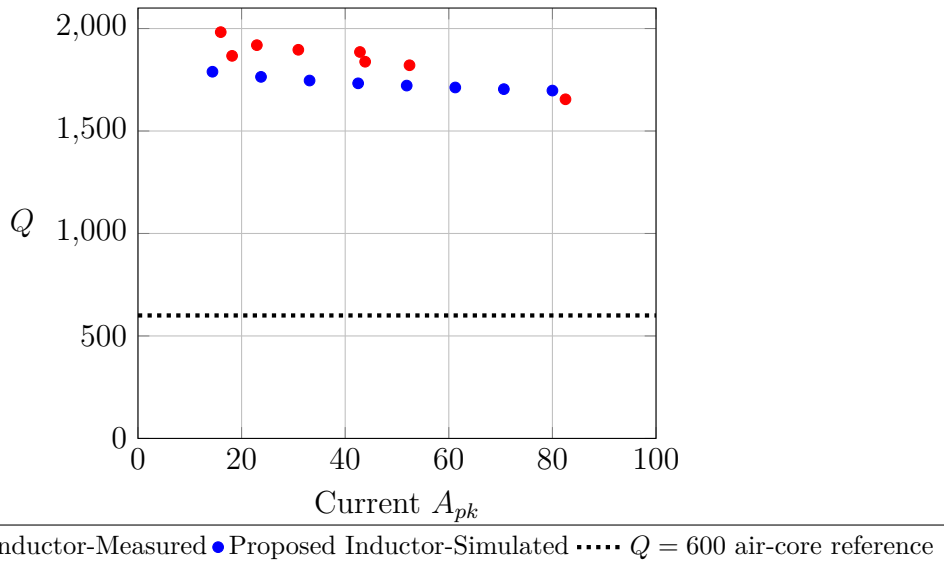
Figure 5-13: Measured and Simulated Inductor Performance at 13.56 MHz as measured with direct single-ended voltage measurements from an oscilloscope. It is noted that these experimental measurements were not repeatable at a later date, and that they are thus suspect.

However, these results were unable to be reliably replicated likely due to the common mode noise and grounding issues covered previously and thus these measurements are suspect.

High current measurements using the voltage doubler technique were unable to be obtained due to conducted EMI causing display instabilities on the Fluke multimeters used to measure the DC voltage. Future work involves eliminating the conducted EMI issue, allowing the voltage doubler to run at the full power. Additionally, the capacitor divider ratio must be changed to reduce the peak output of the voltage doubler (preventing failure of the Schottky diodes). The voltage doubler measurement method obtained a peak quality factor of 1134 at a current of 10.3 A_pk and 13.054 MHz.

5.6   Sources of Discrepancy

One source of discrepancy between the quality factor of a simulated inductor and one measured in the lab is the parasitic capacitance present across the coil leads.

54

(a) Thermal Image of Inductor

(b) Thermal Image of Transformer
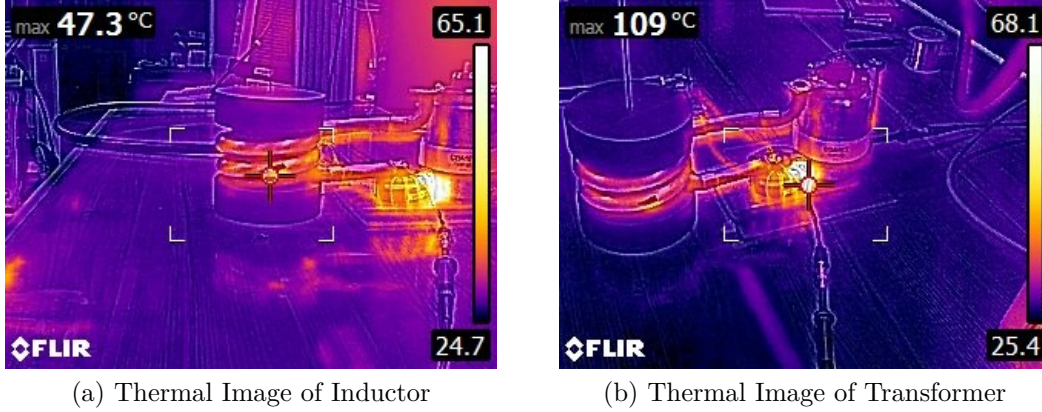
Figure 5-14: Thermal images of Inductor running at nearly full load current. The inductor is carrying 71.2 A_{pk} at 13.404 MHz. These images were captured with a FLIR E6 hand-held thermal camera.
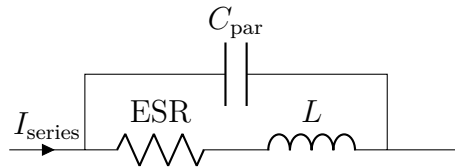
Figure 5-15: Inductor Model Including Parasitic Parallel Capacitance

This capacitance resonates with the main inductor, causing additional currents to flow through the inductor's resistance, inducing additional loss. Illustrated in Fig. 5-15, given a fixed series current I_{series}, additional currents will flow in the LCR loop. Although the loss due to C_{par} is easily calculated[4], the actual capacitance is not. Thus coil simulation tools (such as Coil32) or finite element tools often severely under-predict the quality factor of the inductors they simulate. For reference, Coil 32 estimates the quality factor of the comparison air-coil at 2540, however the peak quality factor obtained was only 1096.

Additionally, several loss mechanisms within the test fixture were not modeled. Fringing fields that exit radially out of the end caps have the potential to impinge on the connecting leads of the test fixture, inducing loss. Interconnect resistances of the solder-connect fittings, contact resistances between the capacitor plates and vacuum capacitor, and the helical nature of the coil were also not modeled.

---

[4]The new Q which accounts for these circulating currents assumes a series R-L circuit where L is the same as inductance as a model which neglects C_{par} and R_{new} is the resistance required to yield the same loss as RLC case. That is, $\frac{I_{\mathrm{series}}^2}{2} R_{\mathrm{new}} = P_{\mathrm{diss,RLC}}$

Finally, at the time of writing, the highest Q factor the voltage doubler RF probe technique is able to measure accurately is not known. As previously shown, quality factors up to 1100 are able to be detected by the doubler however, it is unclear that if an inductor with a quality factor of 1800 is inserted in the system that the voltage doubler will report it as so.

Chapter 6

Self-Shielded Inductor Structure and Design Guidelines

This chapter presents the motivation and design for a fully "self-shielded" inductor for use at radio frequencies (10s of MHz) and high currents (tens of amps).

6.1 Problem Motivation

One pitfall of the proposed distributed gap inductor is the magnetic flux distribution outside of the coils. Without a core piece surrounding the copper coils, flux flows far (radially) away from the inductor. Although this deficiency plagues coreless inductors as well, reducing the flux outside of the core can provide significant performance benefits.

In the RF plasma generation space, there is a very clear desire to miniaturize the boxes that contain these RF power electronics. Miniaturization decreases floor space occupied by the power electronics potentially increasing factory output efficiency. However, there is a strict requirement that all of the power electronics must be placed inside of a metal enclosure in order to reduce electromagnetic interference and loss in surrounding components. Consequently, the size of these enclosures is typically limited by the inductor. If a metal object is placed perpendicularly to a time-varying magnetic field, eddy currents and loss are generated in the metal. This reduces
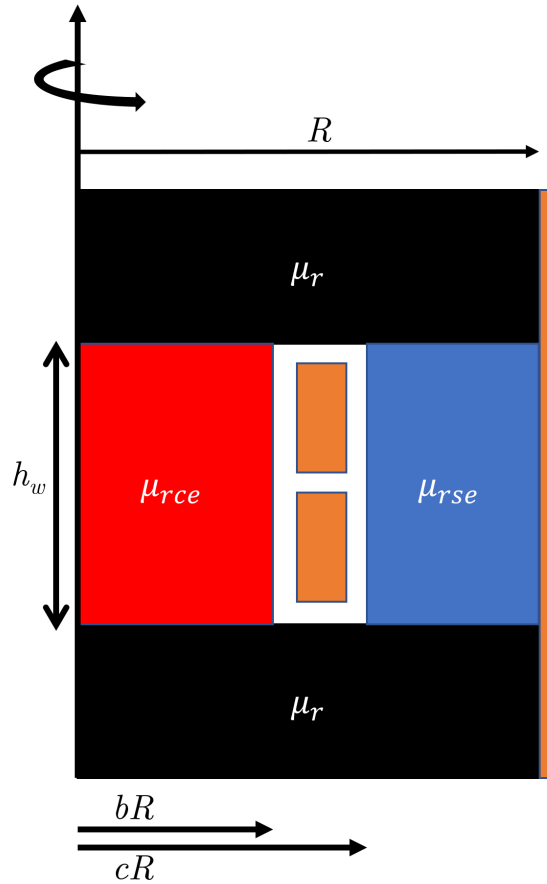
Figure 6-1: Schematic Polar Cutaway of Self-Shielded Inductor

system efficiency, and practically reduces the inductance of the inductor producing the magnetic fields. This is another fundamental flaw in the coreless inductor: the boxes that surround them must be physically large or serious losses will be incurred. Without magnetic materials, there is no way to prevent the magnetic fields from inducing loss in the box.

6.2 Self-Shielded Structure

To solve the aforementioned issues, this section proposes a "self-shielded" structure, so called due to the lack of magnetic fields external to the physical volume of the structure. This shielding is achieved by both including an outer ring of distributed-gap ferrite pieces and wrapping the structure in copper foil. The outer ring of ferrite

provides a shunt path for flux to flow while the copper shield acts as a transference, rejecting any additional flux from flowing outside of the structure. The proposed structure is shown in Fig. 6-1. R is the total radius of the structure (assuming the width of the copper foil as negligible), bR (where b is a number between 0 and 1) represents the radius of the center-post, cR (c also being a number between 0 and 1) is the inner radius of the shell ferrite ring. h_w is the height of window in which the copper turns are placed.

The center and shell ferrite sections are implemented with a distributed gap. μ_{rce} is the relative, effective permeability of the center-post. Calling f_f the fraction of ferrite per unit of distributed gap (i.e. if the height of a single ferrite disc and spacer is 10 mm and the height of the ferrite disc is 5 mm, $f_f = 0.5$), given an effective ferrite permeability $\mu_{r,f}$, μ_{rce} can be calculated:

$$\mathcal{R}_{\text{sum}} = \mathcal{R}_{\text{ferrite}} + \mathcal{R}_{\text{gap}} \tag{6.1}$$

$$\frac{l}{\mu_{r,e}\mu_0 A} = \frac{l_{\text{ferrite}}}{\mu_{r,f}\mu_0 A} + \frac{l_{\text{gap}}}{\mu_0 A} \tag{6.2}$$

$$f_f = \frac{l_{\text{ferrite}}}{l_{\text{ferrite}} + l_{\text{gap}}} \tag{6.3}$$

$$\frac{l}{\mu_{r,e}\mu_0 A} = \left(\frac{f_f}{\mu_{r,f}} + 1 - f_f\right)\frac{l}{\mu_0 A} \tag{6.4}$$

$$\mu_{r,e} = \frac{\mu_{r,f}}{f_f + \mu_{r,f}(1 - f_f)} \tag{6.5}$$

Thus given a desired effective permeability and material permeability, the fraction of ferrite can be calculated (or vice versa). μ_{rse}, the relative effective permeability of the shell, can be calculated similarly.

The magnetic circuit model for the self-shielded design is shown in Fig. 6-2 (Assuming the reluctance of the end caps is negligible).

6.2.1 Scripting and Constraints

Given these definitions, the structure is now generalizable. That is, given the geometries of the ferrite pieces, number of turns, and permeabilities of each ferrite section,
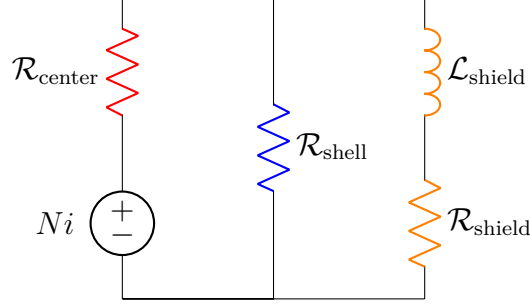
Figure 6-2: Self-Shielded Inductor Magnetic Circuit Model. The lossy nature of the copper shield is modeled with a transference element $\mathcal{L}_{\text{shield}}$ [10].

the inductor structure is fully defined (barring the turn spacing), and able to be tested in FEA software. However, doing rapid design iterations in these types of software is slow and hard to optimize. To solve this, first principle loss and inductance models were developed to enable a brute force search over the solution space. The goal of this brute force search is to minimize total loss subject to inductance and volume constraints. Loss in the copper windings and shield is calculated based on the MMF present on either side of the winding. Assuming that the shield's transference perfectly rejects all flux and that all conduction occurs within a skin depth δ:

$$\mathcal{R}_{\text{center}} = \frac{h_w}{\mu_{rce}\mu_0\pi b^2 R^2} \tag{6.6}$$

$$\mathcal{R}_{\text{shell}} = \frac{h_w}{\mu_{rse}\mu_0\pi R^2(1 - c^2)} \tag{6.7}$$

$$\mathcal{F}_{\text{inner}} = \frac{\mathcal{R}_{\text{center}}}{\mathcal{R}_{\text{center}} + \mathcal{R}_{\text{shell}}} NI \tag{6.8}$$

$$P_{\text{wire,inner}} = \frac{1}{2}\left(\frac{\rho_{cu}2\pi bR}{h\delta}\right)\mathcal{F}_{\text{inner}}^2 \tag{6.9}$$

$$\mathcal{F}_{\text{outer}} = NI - \mathcal{F}_{\text{inner}} \tag{6.10}$$

$$P_{\text{wire,outer}} = \frac{1}{2}\left(\frac{\rho_{cu}2\pi cR}{h\delta}\right)\mathcal{F}_{\text{outer}}^2 \tag{6.11}$$

$$P_{\text{shield}} = \frac{1}{2}\left(\frac{\rho_{cu}2\pi R}{h\delta}\right)\mathcal{F}_{\text{shell}}^2 \tag{6.12}$$

Where $\mathcal{F}_{\text{inner}}$ is the MMF drop across $\mathcal{R}_{\text{center}}$ and $\mathcal{F}_{\text{outer}}$ is the MMF drop across $\mathcal{R}_{\text{outer}}$. Core loss is then calculated using the Steinmetz parameters of the material

and flux density within:

$$B_{\text{center}} = \frac{LI}{N\pi b^2 R^2} \tag{6.13}$$

$$B_{\text{shell}} = \frac{LI}{N\pi(1-c^2)R^2} \tag{6.14}$$

Where I is the peak sinusoidal current carried by the inductor. Using the fraction of ferrite f_f as defined above, an effective Steinmetz coefficient $C_{m,eff} = f_f C_m$ models the layering of ferrite in the center-post and shell:

$$P_{\text{core,center}} = f_{f,\text{center}} C_m f^\alpha B_{\text{center}}^\beta \pi b^2 R^2 h_w \tag{6.15}$$

$$P_{\text{core,shell}} = f_{f,\text{shell}} C_m f^\alpha B_{\text{shell}}^\beta \pi(1-c^2)R^2 h_w \tag{6.16}$$

Where C_m, α and β are the Steinmetz coefficients of the magnetic material to be used. For Fair-rite 67, the Steinmetz coefficients obtained were $C_m = 1.78 \times 10^{-6}$, $\alpha = 2.202$ and $\beta = 2.118$. Finally, loss in the end caps is estimated using the mean radius of the end cap:

$$B_{\text{end cap}} = \frac{LI}{N\pi R h_e} \tag{6.17}$$

$$P_{\text{core,end caps}} = 2C_m f^\alpha B_{\text{end cap}}^\beta \pi R^2 h_e \tag{6.18}$$

Where h_e is the height of a single end cap.

The last equations required for scripting are the two constraints of inductance and volume as a function of the aforementioned parameters. This can be calculated using our simple magnetic circuit model:

$$L = \frac{N^2}{\mathcal{R}_{\text{center}} + \mathcal{R}_{\text{shell}} + 2\mathcal{R}_{\text{endcap}}} \tag{6.19}$$

$$\text{volume} = \pi R^2 (2h_e + h_w) \tag{6.20}$$
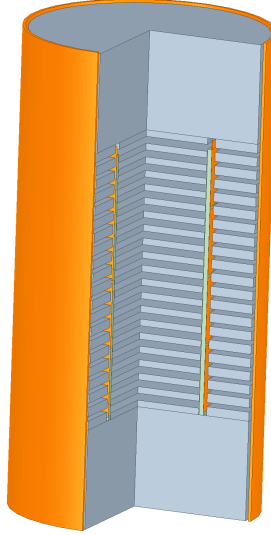
Figure 6-3: 3-D View of Optimal Self-shielded Inductor

Thus we now are able to minimize:

$$\text{Loss} = P_{\text{core,center}} + P_{\text{core,shell}} + P_{\text{wire,inner}} + P_{\text{wire,outer}} + P_{\text{shield}}$$

As a function of the parameters that fully define the inductor as described above. A MATLAB script (Appendix C) was developed to iterate over these parameters via a brute force search method, outputting a design that minimizes the loss of the inductor subject to inductance and volume constraints.

In addition to sweeping the geometries mentioned above, the MMF percentage of the center-post (i.e. $\frac{\mathcal{F}_{\text{center}}}{NI}$) was swept. A higher center-post MMF percentage reduces loss in the shield and the shell ferrite, but increases loss on the inner part of the winding. In an un-shielded design, the optimal center-post MMF percentage is 50% as explained in Section 3.2.2 however with the introduction of the shield losses, the optimal balance was found to be closer to 70 %.

6.3 Results

The output of this brute force script is shown in Fig. 6-3. In addition to the structure outlined above, the inductance was constrained to be 500 nH and the total volume was

	ANSYS	MATLAB
Inductance	623.45 nH	500 nH
Q	1544	1535
Loss Table		
Top End Cap	5.73 W	4.12 W
Bottom End Cap	5.74 W	4.12 W
Shield	7 W	7.71 W
Total Copper Loss	63.81 W	56.21 W
Total Core Loss	46.31 W	32.57 W
Total Loss	110.1 W	88.69 W

Table 6.1: Comparison Between ANSYS and MATLAB Predictions of Self-Shielded Inductor Structure. Although ANSYS reports a higher inductance than predicted by MATLAB, the quality factors are extremely close.

constrained to be 1×10^{-3} m^3. The simulation runs at 13.56 MHz with an excitation current of 80 A_{pk} and a system temperature of 25°C. Fair-rite 67 is used as the core material. The number of gaps was constrained to be 20. Finally the window width (i.e. $R(c - b)$) was constrained to be a minimum of 3.09 mm and the turn-to-turn spacing was 1 mm.

The outer radius of the ferrite is 43 mm, the center-post radius is 23.65 mm. The inner radius of the shell ferrite is 26.74 mm (corresponding to $b = 0.55$ and $c = 0.62$). The center-post distributed gap is made up of 21 pieces of ferrite 2.36 mm tall with center-to-center spacing of 4.89 mm while the shell distributed gap is made of 21 pieces of ferrite 3.27 mm tall with center-to-center spacing of 4.84 mm. The end caps are each 36 mm tall, yielding a total height of 172.15 mm. The total volume of the structure is 0.001 m^3. The center-post MMF percentage is 73.75%. The coil is constructed of 4 turns of 51 μm thick copper 23.79 mm tall with a center-to-center spacing of 24.79 mm. The skin depth of copper at 13.56 MHz and room temperature is approximately 17.7 μm. Thus, in order to maximize the ferrite area (to reduce flux density and thus core loss) the thinnest, easily available copper foil was chosen (2 mil copper foil). A loss table comparing the MATLAB script and ANSYS simulation results is presented in table 6.1.

6.3.1 Distributed Gap Turn Spacing

Per [7], a minimum copper-to-ferrite spacing of $s > 0.25p$ (where s is distance from copper to distributed gap ferrite, in this case radially, and p is the center-to-center spacing of the ferrite pieces) is recommended for reducing fringing field losses induced by the ferrite gaps. Due to this, there is a limit on how small the quantity $c - b$ can be for a given number of distributed gaps. Thus there is a tradeoff between manufacturing complexity and physical volume. Similarly to the inductor proposed in Chapter 3, there is a limit to the mechanical rigidity of short, radially large ferrite discs. Additionally, as will be discussed, mechanical considerations such as how to mount the copper foil within the structure or how to expose the inductor terminals to the "outside world" may limit the proximity of copper to ferrite.

6.4 Future work

6.4.1 Thermal Limitations

Although these initial results are extremely promising, there are several improvements that must be made to the design before it is practical. First, by introducing the copper shield, the "effective" volume of the inductor has been greatly reduced (i.e. the region where there exists considerable magnetic flux produced by the structure). Thus although the physical volume of this structure is approximately the same as the inductor proposed in Chapter 3 (0.001 m^3), the effective volume is significantly smaller and thus the "effective" energy density of the inductor is much higher. This metric manifests itself as higher magnetic flux densities within the ferrite, creating thermal issues. Using a rudimentary ANSYS ICEPACK simulation, the peak temperatures on the center post ferrites were found to be above 200 °C, likely pushing the ferrite into thermal runaway and potentially breaking the ferrite due to the large thermal stress. Although this could be remedied by reducing the peak current carried by the inductor, a rigorous thermal model and cooling solution should be developed to ensure the inductor's success.

6.4.2 End Turn Effects

Second, in the structure proposed above, the copper turns almost entirely fill the window (barring 1 mm spacing between each turn and 1 mm from the end turns to the top and bottom of the ferrite end caps). This is physically unrealizable from a copper coil structure. To wind N turns of wire around a cylinder, the window height must be larger than $(N + 1)$(turn height)$+N$(turn gap height) $+$ 2(turn to ferrite spacing). Thus to make the previously proposed design realizable, the turn height must be reduced significantly. This introduces a variable air gap as a function of θ (within the cylindrical coordinate system of the structure) from the end of each turn to the end caps.

The MATLAB script was modified to account for the reduced conduction area and the inductor re-optimized. A 2-D ANSYS simulation was developed to investigate this effect, where the z-location of the turn within the window (z-offset) was varied, equivalent to sweeping θ in a 3-D structure. Shown in Fig. 6-4, as the turns are moved upwards, the loss within the bottom turn decreases while the loss in the top turn increases. The loss in the three middle turns however, are mostly unaffected by changes in z-position. To simplify the analysis, the inductor in this study was constructed with 100 gaps in both the center-post and shell. It has an outer radius of 39 mm with an end cap height of 30 mm. The radius of the center-post is 21.45 mm with a disc height of 0.851 mm and center-to-center spacing of 1.48 mm. The shell has an inner radius of 24.45 mm with a disc height of 1.028 mm and center-to-center spacing of 1.482 mm. The coil is made of 5 turns of 50 μm copper foil 23.71 mm tall with center-to-center spacing of 24.71 mm.

These "end effects" inhibit the ability of the script to predict the loss and inductance of the simulated inductors accurately. The loss in turn 1 at the highest point is 33.3 W while the maximum loss in turn 2 is only 21 W. These inaccuracies raise doubt on whether or not the output of the brute force search is the truly optimal inductor and thus should be resolved. There are multiple potential solutions to this problem. Instead of using a helical winding structure, a "Z" winding structure can be employed
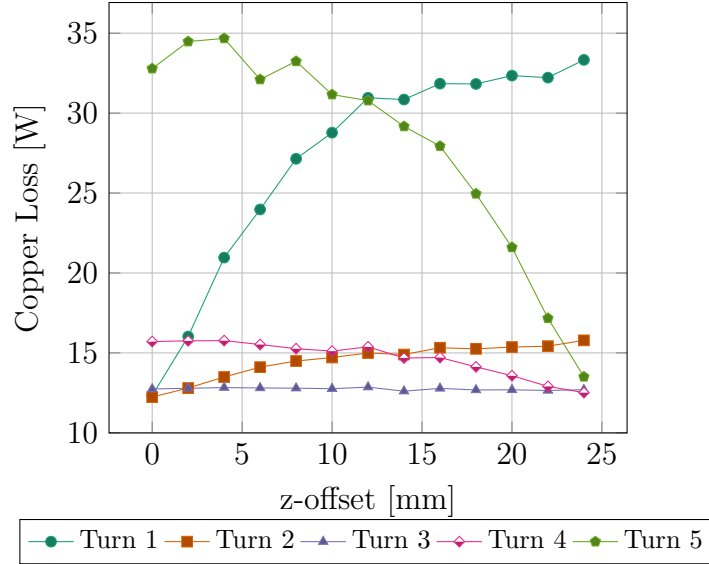
Figure 6-4: Copper Loss By Turn, Sensitivity to z-Position in Window. As the vertical position of the wire within the window is varied, the reluctance of the air gap at either end of the turns changes, inducing variable copper loss. The overall copper loss is maximized at z-offset = 12 mm.

where the turns are mostly continuous bands of copper than make a sudden vertical jump from one turn to the next, forming a Z pattern as one turn turns into the next. This fills more of the window area with copper however suffers from manufacturing complexity and potentially adverse high frequency effects.

Another potential solution is the introduction of un-gapped ferrite in the window area. Illustrated in Fig. 6-5, the ferrite provides a lower reluctance path for flux to flow rather than bypassing the distributed gap and jumping across the air gap in the window. This structure adds another free variable into the optimization plane, h_f (chosen to be the same for all 4 pieces). However, the relationship between the height of these pieces and copper loss is not clear at the time of writing, requiring further study. However, through manual iteration of h_f (constraining all other variables except h_w), some insight can be gathered. Shown in Fig. 6-6 is a study where h_f was set to 0.375 times the height of a single turn (in this case each piece of ferrite in the window area was 7.14 mm tall). Adding the ferrite turns the the loss vs. position relationship from one that is maximal in the middle of the z-offset sweep to one that is minimal, indicating that there is a strong relationship between this added ferrite
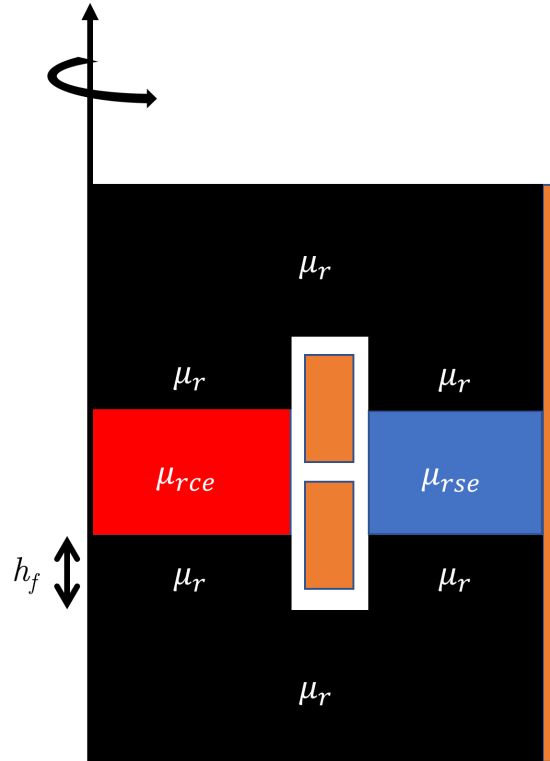
Figure 6-5: Schematic Polar Cutaway of Self-Shielded Inductor with Ungapped Ferrite Added to the Window

piece and the end turn copper loss. N.B., the design used to generate the data in Fig. 6-6 has significantly fewer gaps (10 vs. 100) and a larger window so it is unfair to do a direct 1:1 comparison of the losses in this design with that shown in Fig. 6-4. By fully fleshing out the relationship between h_f and P_{wire}, the inductor can be re-optimized with this new design handle.

6.4.3 Mechanical Design

Finally, the inductor's copper coil structure must be finalized to create a fully man-ufacturable object. The choice of 50 μm copper foil presents a unique challenge to interfacing the inductor with the outside world. Although the thin copper provides more than enough conduction area and maximizes ferrite area, it may not be rigid enough to stand on its on nor sustain reasonable loads that me be imposed by connect-ing terminals. Re-evaluation on the priority of the width of the copper and potential
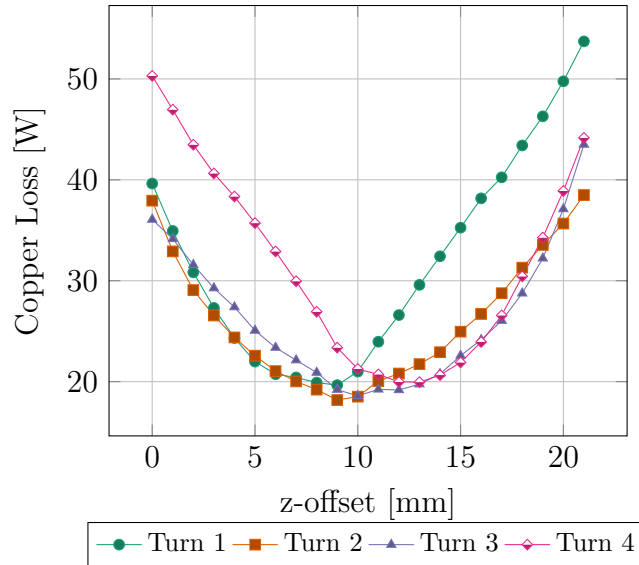
Figure 6-6: Copper Loss By Turn, Sensitivity to z-Position in Window, adding Ungapped Ferrite in Window. The introduction of ungapped ferrite into the window area provides a low reluctance path for flux to flow. Rather than shunting across the air gap, flux is able to continually flow through the ferrite, reducing the adverse interaction between window flux and current within the windings. The overall copper loss is minimized at z-offset = 10 mm.

termination must be investigated. One potential solution to the rigidity issue is using a plastic, low dielectric loss cylinder to affix the copper foil to. Although this necessitates a wider than required window area (thus increasing core loss), it provides a simple method to ensure the concentricity of the copper windings and provides rigidity. Both Teflon and polyethylene are promising plastics for this application due to their strength, low dielectric loss and (relative) inexpensiveness.

Chapter 7

Conclusion

7.1 Key Takeaways

Achieving step changes in the performance of the aforementioned RF systems requires serious thought and engineering. Often the performance of these systems is seriously limited by the magnetics within them. Although the design of high performing magnetic elements is complicated by high frequency effects, this thesis has outlined the mechanisms that limit the efficiency of these elements and methodologies to workaround these limits to the designer's advantage. An example inductor utilizing these design techniques was provided, exhibiting a high though not fully characterized quality factor that is at least 1100 at 20 A_{pk} and may be as high as 1600 at 80 A_{pk}.

Critical to the development of these new design methodologies are the experimental techniques to verify the performance of these magnetic elements in the real world. Given the high levels of performance these design methodologies can achieve, a similarly high performing measurement apparatus is required. The transformer-coupled resonant tank enables the extraction of inductor resistance and thus quality factor at very large drive levels, enabling the next generation of high frequency magnetics. Moreover, an RF probing technique is proposed that can eliminate some of the measurement challenges that were observed in trying to measure the prototype inductor. This technique was validated to be effective, though it will need refinement to be

applied at up to full power levels for these designs.

Finally, an initial proposal and investigation of fully "self-shielded" inductor designs have been presented. This design approach has the potential to not only reduce the system enclosure volume significantly and increase system efficiency, but enable greater system flexibility as designers are no longer constrained by the large fringing magnetic fields produced by conventional air-core solenoids and the associated coupling with other circuit elements

7.2   Future Work

Complete characterization of the proposed inductor will be necessary to ensure its practicality and widespread adoption. How the inductor behaves under steady-state, high power operation (e.g. hot spot temperatures, quality factor degradation vs. temperature), will quell the concerns that the non-linear ferrite material raises. Finalizing the measurement apparatus to enable high current testing with the voltage doubler strategy is critical to this goal. Finally, a complete understanding of the common mode currents issue may be necessary as more complicated systems are designed and manufactured where loss is at a premium.

Work on the self-shielded design has only just begun. Fully fleshed out magnetics and thermal modeling will enable stronger designs that push the physical limits of this design space. Additionally, finalizing the mechanical design will be required to make an inductor that looks good in simulation into one that looks amazing in the real world.

Although much of this thesis has focused on HF AC inductor design, extensions to other magnetic elements such as transformers and inductors which carry both DC and HF AC currents are apparent. Both of these design spaces present significant and different challenges to the ones explored in this thesis but are pivotal to the success of many power electronics applications.

Appendix A

Magnetic Materials Performance Factor Code

```matlab
close all
clear all
clc

file ='Material Data.xlsx';
figure()
X_fit = [1, 100];
X_fit_log = log(X_fit);

%% Start of HRM 40
B_1A = xlsread(file,3,'T20:T24');
P_1A = xlsread(file,3,'U20:U24');


fit_1A = polyfit(log(B_1A),log(P_1A),1);


B_2A = xlsread(file,3,'T13:T17');
P_2A = xlsread(file,3,'U13:U17');


fit_2A = polyfit(log(B_2A),log(P_2A),1);

```

```matlab
B_3A = xlsread(file,3,'T5:T9');
P_3A = xlsread(file,3,'U5:U9');
fit_3A = polyfit(log(B_3A),log(P_3A),1);


perf1A=exp((log(500)-fit_1A(2))/fit_1A(1));
perf2A=exp((log(500)-fit_2A(2))/fit_2A(1));
perf3A = exp((log(500)-fit_3A(2))/fit_3A(1));
freqA=[2.8,5.9,10.1];
perf_yA=[perf1A*freqA(1),perf2A*freqA(2),perf3A*freqA(3)];
%%Start of NL-12S
B_1B = xlsread(file,4,'V44:V47');
P_1B = xlsread(file,4,'W44:W47');
fit_1B = polyfit(log(B_1B),log(P_1B),1);


B_2B = xlsread(file,4,'V37:V41');
P_2B = xlsread(file,4,'W37:W41');
fit_2B = polyfit(log(B_2B),log(P_2B),1);


B_3B = xlsread(file,4,'V50:V54');
P_3B = xlsread(file,4,'W50:W54');
fit_3B = polyfit(log(B_3B),log(P_3B),1);


perf1B=exp((log(500)-fit_1B(2))/fit_1B(1));
perf2B=exp((log(500)-fit_2B(2))/fit_2B(1));
perf3B = exp((log(500)-fit_3B(2))/fit_3B(1));
freqB=[2.9,5.9,10.2];
perf_yB=[perf1B*freqB(1),perf2B*freqB(2),perf3B*freqB(3)];
%Start of ML95S
B_1C = xlsread(file,5,'V5:V8');
P_1C = xlsread(file,5,'W5:W8');
fit_1C = polyfit(log(B_1C),log(P_1C),1);


B_2C = xlsread(file,5,'V11:V14');
P_2C = xlsread(file,5,'W11:W14');
fit_2C = polyfit(log(B_2C),log(P_2C),1);
```

```matlab
56
57   B_3C = xlsread(file,5,'V16:V19');
58   P_3C = xlsread(file,5,'W16:W19');
59   fit_3C = polyfit(log(B_3C),log(P_3C),1);
60
61   perf1C=exp((log(500)-fit_1C(2))/fit_1C(1));
62   perf2C=exp((log(500)-fit_2C(2))/fit_2C(1));
63   perf3C = exp((log(500)-fit_3C(2))/fit_3C(1));
64   freqC=[2,1,.58];
65   perf_yC=[perf1C*freqC(1),perf2C*freqC(2),perf3C*freqC(3)];
66   %Start of NL-X9
67   B_1D = xlsread(file,2,'T5:T10');
68   P_1D = xlsread(file,2,'U5:U10');
69   fit_1D = polyfit(log(B_1D),log(P_1D),1);
70
71   B_2D = xlsread(file,2,'T18:T21');
72   P_2D = xlsread(file,2,'U18:U21');
73   fit_2D = polyfit(log(B_2D),log(P_2D),1);
74
75   B_3D = xlsread(file,2,'T26:T30');
76   P_3D = xlsread(file,2,'U26:U30');
77   fit_3D = polyfit(log(B_3D),log(P_3D),1);
78
79   % B_4D = xlsread(file,2,'T33:T37');
80   % P_4D = xlsread(file,2,'U33:U37');
81   % fit_4D = polyfit(log(B_4D),log(P_4D),1); 11.4 MHz was bad data
82
83   B_5D = xlsread(file,2,'T46:T51');
84   P_5D = xlsread(file,2,'U46:U51');
85   fit_5D = polyfit(log(B_5D),log(P_5D),1);
86
87   B_6D = xlsread(file,2,'T40:T43');
88   P_6D = xlsread(file,2,'U40:U43');
89   fit_6D = polyfit(log(B_6D),log(P_6D),1);
90
```

```matlab
91   perf1D=exp((log(500)-fit_1D(2))/fit_1D(1));
92   perf2D=exp((log(500)-fit_2D(2))/fit_2D(1));
93   perf3D = exp((log(500)-fit_3D(2))/fit_3D(1));
94   % perf4D = exp((log(500)-fit_4D(2))/fit_4D(1));
95   perf5D = exp((log(500)-fit_5D(2))/fit_5D(1));
96   perf6D = exp((log(500)-fit_6D(2))/fit_6D(1));
97   freqD=[3,6,10,10.8,15];
98   perf_yD=[perf1D*freqD(1),perf2D*freqD(2),perf3D*freqD(3),perf6D*freqD(4),perf5D*
     ↪  freqD(5)];
99   %start of ML91S
100  B_1E = xlsread(file,6,'V5:V8');
101  P_1E = xlsread(file,6,'W5:W8');
102  fit_1E = polyfit(log(B_1E),log(P_1E),1);
103
104  B_4E = xlsread(file,6,'V32:V36');
105  P_4E = xlsread(file,6,'W32:W36');
106  fit_2E = polyfit(log(B_4E),log(P_4E),1);
107
108  B_3E = xlsread(file,6,'V11:V14');
109  P_3E = xlsread(file,6,'W11:W14');
110  fit_3E = polyfit(log(B_3E),log(P_3E),1);
111
112  B_2E=xlsread(file,6,'V17:V21');
113  P_2E=xlsread(file,6,'W17:W21');
114  fit_4E= polyfit(log(B_2E),log(P_2E),1);
115
116  B_5E=xlsread(file,6,'V39:V44');
117  P_5E=xlsread(file,6,'W39:W44');
118  fit_5E= polyfit(log(B_5E),log(P_5E),1);
119
120  perf1E=exp((log(500)-fit_1E(2))/fit_1E(1));
121  perf2E=exp((log(500)-fit_2E(2))/fit_2E(1));
122  perf3E = exp((log(500)-fit_3E(2))/fit_3E(1));
123  perf4E= exp((log(500)-fit_4E(2))/fit_4E(1));
124  perf5E=exp((log(500)-fit_5E(2))/fit_5E(1));
```

```matlab
125    freqE=[5,4,3,2,1];
126    perf_yE=[perf1E*freqE(1),perf2E*freqE(2),perf3E*freqE(3),perf5E*freqE(4),perf4E*
       ↪   freqE(5)];
127    %Start of ML-X6A
128    B_1F=xlsread(file,7,'V5:V11');
129    P_1F=xlsread(file,7,'W5:W11');
130    fit_1F=polyfit(log(B_1F),log(P_1F),1);
131
132    B_2F=xlsread(file,7,'V14:V18');
133    P_2F=xlsread(file,7,'W14:W18');
134    fit_2F=polyfit(log(B_2F),log(P_2F),1);
135
136    B_3F=xlsread(file,7,'V21:V25');
137    P_3F=xlsread(file,7,'W21:W25');
138    fit_3F=polyfit(log(B_3F),log(P_3F),1);
139
140    perf1F=exp((log(500)-fit_1F(2))/fit_1F(1));
141    perf2F=exp((log(500)-fit_2F(2))/fit_2F(1));
142    perf3F=exp((log(500)-fit_3F(2))/fit_3F(1));
143    freqF=[2,1,.66];
144    perf_yF=[perf1F*freqF(1),perf2F*freqF(2),perf3F*freqF(3)];
145    %Start of ML-29D
146    B_1G=xlsread(file,8,'V5:V10');
147    P_1G=xlsread(file,8,'W5:W10');
148    fit_1G=polyfit(log(B_1G),log(P_1G),1);
149
150    perf1G=exp((log(500)-fit_1G(2))/fit_1G(1));
151    freqG=[.9];
152    perf_yG=[perf1G*freqG(1)];
153    %Start of NEC Tokin Mystery Material
154    B_1H=xlsread(file,9,'V5:V11');
155    P_1H=xlsread(file,9,'W5:W11');
156    fit_1H=polyfit(log(B_1H),log(P_1H),1);
157
158    B_2H=xlsread(file,9,'V14:V18');
```

```matlab
159    P_2H=xlsread(file,9,'W14:W18');
160    fit_2H=polyfit(log(B_2H),log(P_2H),1);
161
162    B_3H=xlsread(file,9,'V32:V35');
163    P_3H=xlsread(file,9,'W32:W35');
164    fit_3H=polyfit(log(B_3H),log(P_3H),1);
165
166    perf1H=exp((log(500)-fit_1H(2))/fit_1H(1));
167    perf2H=exp((log(500)-fit_2H(2))/fit_2H(1));
168    perf3H=exp((log(500)-fit_3H(2))/fit_3H(1));
169    freqH=[10,3,1];
170    perf_yH=[perf1H*freqH(1),perf2H*freqH(2),perf3H*freqH(3)];
171    %Start of Fi 150
172    B_1I=xlsread(file,10,'V5:V9');
173    P_1I=xlsread(file,10,'W5:W9');
174    fit_1I=polyfit(log(B_1I),log(P_1I),1);
175
176    B_2I=xlsread(file,10,'V12:V15');
177    P_2I=xlsread(file,10,'W12:W15');
178    fit_2I=polyfit(log(B_2I),log(P_2I),1);
179
180    B_3I=xlsread(file,10,'V18:V21');
181    P_3I=xlsread(file,10,'W18:W21');
182    fit_3I=polyfit(log(B_3I),log(P_3I),1);
183
184    perf1I=exp((log(500)-fit_1I(2))/fit_1I(1));
185    perf2I=exp((log(500)-fit_2I(2))/fit_2I(1));
186    perf3I=exp((log(500)-fit_3I(2))/fit_3I(1));
187
188    freqI=[10,6,3];
189    perf_yI=[perf1I*freqI(1),perf2I*freqI(2),perf3I*freqI(3)];
190    %Start Fi 130
191    B_1J=xlsread(file,11,'V5:V8');
192    P_1J=xlsread(file,11,'W5:W8');
193    fit_1J=polyfit(log(B_1J),log(P_1J),1);
```

```matlab
194
195  B_2J=xlsread(file,11,'V12:V15');
196  P_2J=xlsread(file,11,'W12:W15');
197  fit_2J=polyfit(log(B_2J),log(P_2J),1);
198
199  B_3J=xlsread(file,11,'V18:V20');
200  P_3J=xlsread(file,11,'W18:W20');
201  fit_3J=polyfit(log(B_3J),log(P_3J),1);
202
203  perf1J=exp((log(500)-fit_1J(2))/fit_1J(1));
204  perf2J=exp((log(500)-fit_2J(2))/fit_2J(1));
205  perf3J=exp((log(500)-fit_3J(2))/fit_3J(1));
206
207  freqJ=[10,6,3];
208  perf_yJ=[perf1J*freqJ(1),perf2J*freqJ(2),perf3J*freqJ(3)];
209  %% Start of 3F46
210  B_1K=xlsread(file,12,'V5:V9');
211  P_1K=xlsread(file,12,'W5:W9');
212  fit_1K=polyfit(log(B_1K),log(P_1K),1);
213
214  B_2K=xlsread(file,12,'V12:V15');
215  P_2K=xlsread(file,12,'W12:W15');
216  fit_2K=polyfit(log(B_2K),log(P_2K),1);
217
218  B_3K=xlsread(file,12,'V18:V21');
219  P_3K=xlsread(file,12,'W18:W21');
220  fit_3K=polyfit(log(B_3K),log(P_3K),1);
221
222  B_4K=xlsread(file,12,'V36:V39');
223  P_4K=xlsread(file,12,'W36:W39');
224  fit_4K=polyfit(log(B_4K),log(P_4K),1);
225
226  B_5K=xlsread(file,12,'V42:V46');
227  P_5K=xlsread(file,12,'W42:W46');
228  fit_5K=polyfit(log(B_5K),log(P_5K),1);
```

```matlab
229
230    B_6K=xlsread(file,12,'V49:V51');
231    P_6K=xlsread(file,12,'W49:W51');
232    fit_6K=polyfit(log(B_6K),log(P_6K),1);
233
234    perf1K=exp((log(500)-fit_1K(2))/fit_1K(1));
235    perf2K=exp((log(500)-fit_2K(2))/fit_2K(1));
236    perf3K=exp((log(500)-fit_3K(2))/fit_3K(1));
237    perf4K=exp((log(500)-fit_4K(2))/fit_4K(1));
238    perf5K=exp((log(500)-fit_5K(2))/fit_5K(1));
239    perf6K=exp((log(500)-fit_6K(2))/fit_6K(1));
240    freqK=[6,3,2,1];
241    perf_yK=[perf1K*freqK(1),perf2K*freqK(2),perf4K*freqK(3),perf3K*freqK(4)];
242    %% 3F46 Double Stack
243    B_1L=xlsread(file,13,'W5:W8');
244    P_1L=xlsread(file,13,'X5:X8');
245    fit_1L=polyfit(log(B_1L),log(P_1L),1);
246
247    B_2L=xlsread(file,13,'W11:W14');
248    P_2L=xlsread(file,13,'X11:X14');
249    fit_2L=polyfit(log(B_2L),log(P_2L),1);
250
251    B_3L=xlsread(file,13,'W41:W46');
252    P_3L=xlsread(file,13,'X41:X46');
253    fit_3L=polyfit(log(B_3L),log(P_3L),1);
254
255    perf1L=exp((log(500)-fit_1L(2))/fit_1L(1));
256    perf2L=exp((log(500)-fit_2L(2))/fit_2L(1));
257    perf3L=exp((log(500)-fit_3L(2))/fit_3L(1));
258
259    freqL=[1,2,3];
260    perf_yL=[perf1L*freqL(1),perf2L*freqL(2),perf3L*freqL(3)];
261
262    %% Start of Hanson Performance Factor
263    HfreqA = [.02,.1,.2,.25,.4,.5,.6,.8,1,1.5,3,4,5,6];
```

```matlab
264    HperfA = [10,30,38,39,41,45,51,58,60,63,70,70,75,80];

265

266    HfreqB =[2,4.5,7,9.8,13,17,20];

267    HperfB = [68,100,115,140,138,140,137];

268    %% Start of Anna Data

269    anna_file ='../Anna/Data_calculations_graph';

270    AB_1A = xlsread(anna_file,4,'P57:P66');

271    AP_1A = xlsread(anna_file,4,'Q57:Q66');

272    Afit_1A = polyfit(log(AB_1A),log(AP_1A),1);

273

274    AB_2A = xlsread(anna_file,4,'P68:P75');

275    AP_2A = xlsread(anna_file,4,'Q68:Q75');

276    Afit_2A = polyfit(log(AB_2A),log(AP_2A),1);

277

278    AB_3A = xlsread(anna_file,4,'P33:P39');

279    AP_3A = xlsread(anna_file,4,'Q33:Q39');

280    Afit_3A = polyfit(log(AB_3A),log(AP_3A),1);

281

282    AB_4A = xlsread(anna_file,4,'P14:P21');

283    AP_4A = xlsread(anna_file,4,'Q14:Q21');

284    Afit_4A = polyfit(log(AB_4A),log(AP_4A),1);

285

286    Aperf1A=exp((log(500)-Afit_1A(2))/Afit_1A(1));

287    Aperf2A=exp((log(500)-Afit_2A(2))/Afit_2A(1));

288    Aperf3A = exp((log(500)-Afit_3A(2))/Afit_3A(1));

289    Aperf4A = exp((log(500)-Afit_4A(2))/Afit_4A(1));

290    AfreqA=[6,5,3,1];

291    Aperf_yA=[Aperf1A*AfreqA(1),Aperf2A*AfreqA(2),Aperf3A*AfreqA(3),Aperf4A*AfreqA(4
    ↪ )];

292

293    AB_1B = xlsread(anna_file,5,'P32:P40');

294    AP_1B = xlsread(anna_file,5,'Q32:Q40');

295    Afit_1B = polyfit(log(AB_1B),log(AP_1B),1);

296

297    AB_2B = xlsread(anna_file,5,'P23:P31');
```

```matlab
298    AP_2B = xlsread(anna_file,5,'Q23:Q31');
299    Afit_2B = polyfit(log(AB_2B),log(AP_2B),1);
300
301    AB_3B = xlsread(anna_file,5,'P5:P12');
302    AP_3B = xlsread(anna_file,5,'Q5:Q12');
303    Afit_3B = polyfit(log(AB_3B),log(AP_3B),1);
304
305    AB_4B = xlsread(anna_file,5,'P13:P22');
306    AP_4B = xlsread(anna_file,5,'Q13:Q22');
307    Afit_4B = polyfit(log(AB_4B),log(AP_4B),1);
308
309    Aperf1B=exp((log(500)-Afit_1B(2))/Afit_1B(1));
310    Aperf2B=exp((log(500)-Afit_2B(2))/Afit_2B(1));
311    Aperf3B = exp((log(500)-Afit_3B(2))/Afit_3B(1));
312    Aperf4B = exp((log(500)-Afit_4B(2))/Afit_4B(1));
313    AfreqB=[6,5,3,1];
314    Aperf_yB=[Aperf1B*AfreqB(1),Aperf2B*AfreqB(2),Aperf3B*AfreqB(3),Aperf4B*AfreqB(4
    ↪  )];
315    %% Graphs
316    semilogx(freqA,perf_yA,"-ro","Linewidth", 3);
317    hold on
318    semilogx(freqB,perf_yB,"-bo","Linewidth", 3);
319    hold on
320    semilogx(freqC,perf_yC,"-mo","Linewidth", 3);
321    hold on
322    semilogx(freqD,perf_yD,"-ko","Linewidth", 3);
323    hold on
324    semilogx(freqE,perf_yE,"-o","Linewidth", 3);
325    hold on
326    semilogx(freqF,perf_yF,"-o","Linewidth",3);
327    hold on
328    semilogx(freqG,perf_yG,"-o","Linewidth",3);
329    hold on
330    semilogx(freqH,perf_yH,"-o","Linewidth",3);
331    hold on
```

```matlab
332    semilogx(freqI,perf_yI,"-o","Linewidth",3);
333    hold on
334    semilogx(freqJ,perf_yJ,"-o","Linewidth",3);
335    hold on
336    semilogx(freqK,perf_yK,"-o","Linewidth",3);
337    hold on
338    semilogx(freqL,perf_yL,"-o","Linewidth",3);
339    hold on
340
341    semilogx(HfreqA,HperfA,"--+","Linewidth", 3);
342    hold on
343    semilogx(HfreqB,HperfB,"--+","Linewidth", 3);
344    hold on
345
346    semilogx(AfreqA,Aperf_yA,"-d","Linewidth", 2);
347    hold on
348    semilogx(AfreqB,Aperf_yB,"-d","Linewidth", 2);
349    title("Performance Factors","Fontsize", 24);
350    xlabel("Frequency (MHz)","Fontsize", 24);
351    ylabel("Performance Factor (mT*MHz)","Fontsize",24);
352    leg=legend("HRM-40","NL-12S","ML95S","NL-X9","ML91S","ML-X6A","ML-29D","NEC
    ↪    Token Mystery","Fi 150", "Fi 130","3F46","3F46 Double Stacked","Hanson
    ↪    Ferrox. [28]","Hanson 67","80","Anna EPCOS");
353    set( leg,'Fontsize',24,'Location','west');
354    set(gca,'xticklabel',[0.01 0.1 1 10 100],'Fontsize', 18);
355    grid on
```

Appendix B

High Power Inductor Python Script

```python
import math


u0 = 1.257e-6    # permeability of free space in [H/m]
Fv = 0.6         # vertical fill factor of winding in window (can range from 0 to
↪  1, recommended range from 0.5 to 0.8)
Fh = 1.0         # horizontal fill factor of winding in window (can range from 0
↪  to 1, recommended range from 0.4 to 0.6)
ratio = 0.9      # aspect ratio (defined as diameter/height)


# input variables
uc = 40.         # relative permeability of core material
L = 500e-9       # desired inductance in [H]
#vol = 1.16e-3  # desired volume in [m^3]
N = 2            # number of turns
Ng=10        # number of gaps


if __name__ == '__main__':
    # compute total radius based on fringing field reluctance approximation
    # Rf = .9 / (u0*math.pi*rt)
    Rf_min=N**2/(2*L)
```

```python
19
20          '''
21          if vol>(.9 * (2*math.pi)**(1/3) * 1/(u0*math.pi*Rf_min * (ratio)**(1/3) )
    ↪    )**3:
22              print("This will not work, fringing reluctance too small!\n")
23              print("Max volume is:"+str((.9 * (2*math.pi)**(1/3) *
    ↪    1/(u0*math.pi*Rf_min * (ratio)**(1/3) ) )**3)+" m^3")
24              exit()
25          '''
26          rt=.9*2*L/(N**2*u0*math.pi)
27          #ht=vol/(math.pi*rt**2)
28          ht=rt*2/ratio
29          h=rt/(.67*math.exp(.5*N)) #optimal approximation for end cap height
30          # compute wire diameter (Dw) to achieve desired vertical window fill (Fv)
             ↪    (Section III-D)
31          Dw = (ht - 2.*h) * Fv / N
32          # computer window width (w) to achieve desired horizontal window fill (Fh)
             ↪    (Section III-E)
33          w = Dw / Fh
34          rc=rt-w #centerpost radius
35          Lg=.9*rc**2/rt #Total gap length to math reluctance
36          hdisc=(ht-2*h-Lg)/(Ng+1)
37          lg=Lg/Ng #individual gap length
38          # center to center disk spacing
39          CC_disk = lg+hdisc
40          vol=math.pi*rt**2*ht
41
42          print("GEOMETRIC PARAMETERS FOR L = ", L, "H, volume = ", vol, "m^3")
43          print("Total height: ",round(ht*1000,3),"mm")
44          print("Total radius: ",round(rt*1000,3),"mm")
45          print("End cap height: ",round(h*1000,3),"mm")
46          print("Disc radius: ",round(rc*1000,3),"mm")
47          print("Disc height: ",round(hdisc*1000,3),"mm")
48          print("Center to center disk spacing: ",round(CC_disk*1000,3),'mm')
49          print("Ng: ",Ng)
```

84

```python
50      print("Total height shoud be: " ,round(ht*1000,3), "mm")
51      print("WIRE SPECS: ")
52      print("Place wire center at x = ", round((Dw/2+rc+CC_disk/4)*1000,3), "mm &
   ↪  z = ", round((h+(ht-2*h)/(N+1)) * 1000,3), "mm")
53      print("Wire radius: ",  round(Dw/2*1000,3),"mm")
54      print("Center to center wire spacing: ",round((ht-2*h)/(N+1)*1000,3), "mm")
```

Appendix C

Shielded Inductor Script

```matlab
clearvars
close all

u_0 = 4*pi*1e-7; %Permeability of free space
I = 80; %Peak current exciation
f = 13.56e6; %Excitation frequency [Hz]
L = 500e-9; %Desired inductance [H]
vol = 1e-3; %Desired volume [m^3]
rho_cu = 1.8e-8; %Resistivity of copper at 25 C
delta = sqrt(rho_cu/(pi*u_0*f)); %Skin depth
N_g = 10; %Number of desired gaps
l_turn_gap = 1e-3; %Gap b/t adjacent turns

% FR 67 Parameters
u_f = 40; %Relative permeability of ferrite
C_m = 1.77925e-6; %P_cv = C_m*f^alpha*B^beta [W/m^3]
alpha = 2.202496; %steinmetz freq. param, X in ANSYS
beta = 2.118208; %steinmetz b-field param, Y in ANSYS

P_min = 1e6;

for N = 1:1:6
    fprintf("N: %d\r\n", N)
```

```matlab
for R = 5e-3:1e-3:150e-3
    for h_e = 5e-3:1e-3:200e-3 %end cap height
        h_w = vol/(pi*R^2)-2*h_e;
        cond_area = N*delta/(N+1)*(h_w-(N+2)*l_turn_gap);
        if(h_w<l_turn_gap*(N+2))
            continue
        end
        for b = 0.1:.01:1
            for c = 20e-3/R+b:0.01:1
                for F_c = 0:N*I
                    P_cu = rho_cu*pi*R*(b*F_c.^2/cond_area+(I*N-F_c).^2.*(c/|
                        ↪  cond_area+1/(delta*h_w)));
                    R_e = R/(pi*R*h_e*u_f*u_0); %Reluctance of end cap
                    R_c = N*F_c/(L*I); %Reluctance of center post
                    u_rce = h_w/(R_c*pi*b^2*R^2*u_0); %Effective relative
                        ↪  permeability of center post
                    f_fc = u_f/(u_rce)*(u_rce-1)/(u_f-1); %Fraction of
                        ↪  ferrite in center post required to achieve u_rce
                    B_c = L*I/(N*pi*b^2*R^2); %Flux density in the center
                        ↪  post
                    P_core_c = (f_fc*C_m)*f^alpha*B_c^beta*pi*b^2*R^2*h_w;
                        ↪  %Core loss in center post [W]
                    R_s = N^2/L-R_c-2*R_e; %Shell reluctance required to hit
                        ↪  F_c, L requirement
                    u_rse = h_w/(R_s*pi*R^2*(1-c^2)*u_0); %Effective
                        ↪  relative permeability of shell
                    f_fs =  u_f/(u_rse)*(u_rse-1)/(u_f-1); %fraction of
                        ↪  ferrite in shell required to achieve u_rse
                    B_s = L*I/(N*pi*R^2*(1-c^2)); %Flux density in shell
                    P_core_s = f_fs*C_m*f^alpha*B_s^beta*pi*R^2*(1-c^2)*h_w;
                        ↪  %Core loss in shell [W]
                    B_end = L*I/(N*pi*R*h_e); %Flux density in end caps
                    P_core_end = 2*C_m*f^alpha*B_end^beta*pi*R^2*h_e; %Core
                        ↪  loss in end caps
                    P_tot = P_core_s+P_core_c+P_cu+P_core_end;
```

```matlab
                              if(P_tot<P_min && P_tot>0)
                                  P_min = P_tot;
                                  P_cu_min = P_cu;
                                  P_core_min = P_core_s+P_core_c+P_core_end;
                                  P_core_s_min = P_core_s;
                                  P_core_c_min = P_core_c;
                                  P_core_end_min = P_core_end;
                                  P_shield_min =
                                  ↪  1/(2*h_w*delta)*rho_cu*2*pi*R*(N*I-F_c)^2;
                                  b_min = b;
                                  c_min = c;
                                  F_c_min = F_c;
                                  N_min = N;
                                  u_rse_min = u_rse;
                                  u_rce_min = u_rce;
                                  f_fs_min = f_fs;
                                  f_fc_min = f_fc;
                                  R_min = R;
                                  h_e_min = h_e;
                                  fprintf("Current P_min: %0.2f [W]\r\n",P_tot)
                              end
                          end
                      end
                  end
              end
          end
      end

Q = 2*pi*f*.5*L*I^2/(P_min);

h_w_min = vol/(pi*R_min^2)-2*h_e_min;
cond_area_min = N_min*delta/(N_min+1)*(h_w_min-(N_min+2)*l_turn_gap);
clc

fprintf("P_min: %0.3f [W]\r\n",P_min);
```

89

```matlab
83    fprintf("N: %0.1f\r\n",N_min);
84    fprintf("Q: %0.f\r\n",Q)
85    fprintf("Center-post MMF percentage: %0.2f [%%]\r\n",100*F_c_min/(N_min*I))
86    fprintf("Outer Radius: %0.2f [mm]\r\n",1e3*R_min)
87    fprintf("End Cap height: %0.2f [mm]\r\n",1e3*h_e_min)
88    fprintf("Center-post radius: %0.2f [mm]\r\n",1e3*b_min*R_min);
89    fprintf('Center disc height: %0.7f
   ↪   [mm]\r\n',1e3*f_fc_min*h_w_min/(N_g*(1-f_fc_min)+f_fc_min*(1+N_g)));
90    fprintf("Shell thickness: %0.2f [mm]\r\n",1e3*(1-c_min)*R_min);
91    fprintf('Shell disc height: %0.7f
   ↪   [mm]\r\n',1e3*f_fs_min*h_w_min/(N_g*(1-f_fs_min)+f_fs_min*(1+N_g)));
92    fprintf('Center gap pitch: %0.7f [mm]\r\n',1e3*f_fc_min*h_w_min/(N_g*(1-f_fc_min⌋
   ↪   )+f_fc_min*(1+N_g))*1/f_fc_min);
93    fprintf('Shell gap pitch: %0.7f [mm]\r\n',1e3*f_fs_min*h_w_min/(N_g*(1-f_fs_min)⌋
   ↪   +f_fs_min*(1+N_g))*1/f_fs_min);
94    fprintf('Copper height with 1 mm turn spacing: %0.4f [mm]\r\n',
   ↪   1e3*(h_w_min-l_turn_gap*(N_min+2))/(N_min+1));
```

Appendix D

Capacitor Divider PCB

The PCB is made of Rogers 4350B substrate manufactured by MyroPCB. Mechanical dimensions shown in the following documents are in mil.

Mica Capacitors

INPUT

| C1 5pF | C2 5pF | C3 5pF | C4 5pF | C5 5pF | C6 5pF | C7 5pF | C8 5pF | C9 5pF | C10 5pF |

PROBE

ID1
PK106-4

C11
Cap Semi
20pF

GND
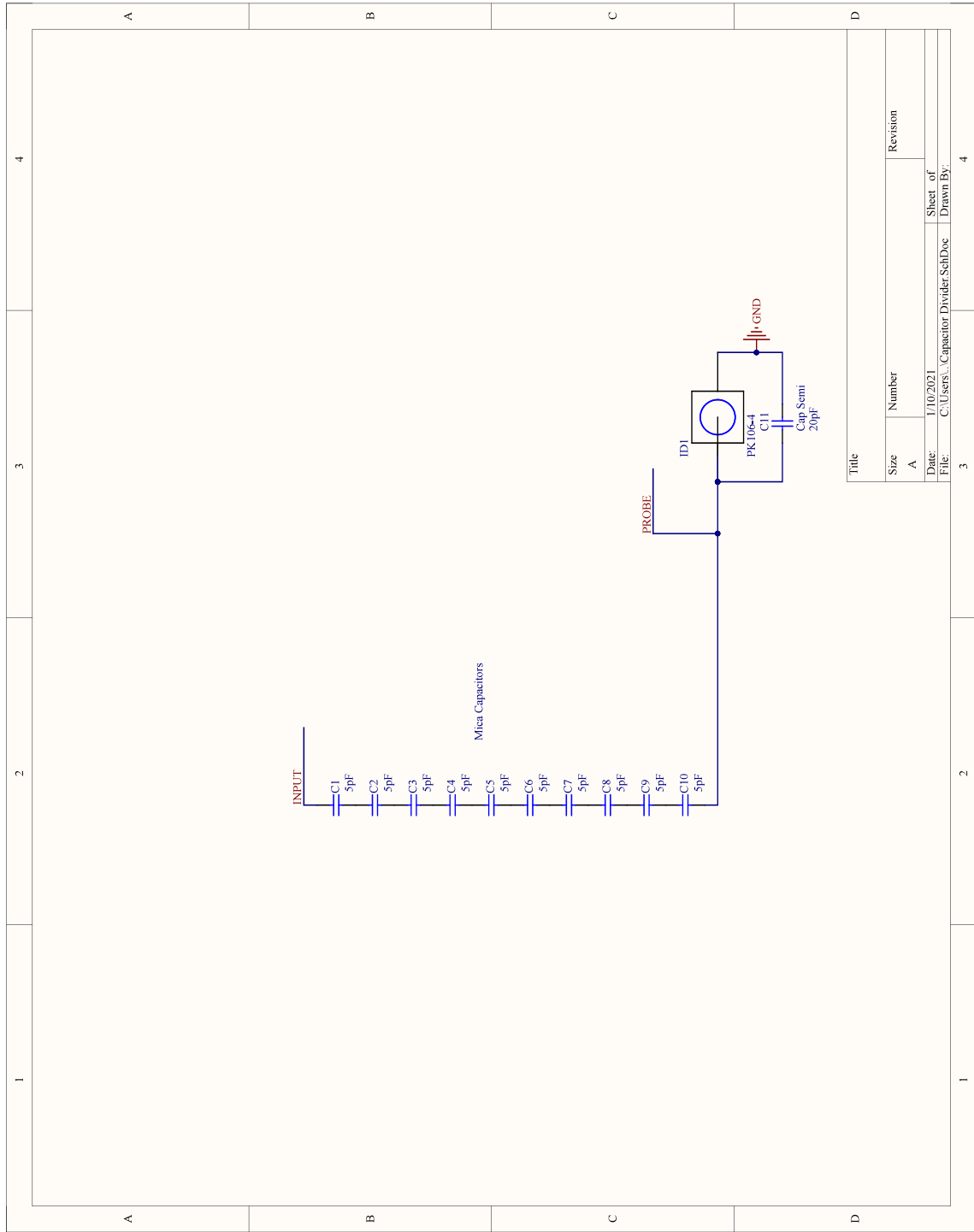
Title

Size Number   Revision
A

Date: 1/10/2021   Sheet of
File: C:\Users\...\Capacitor Divider.SchDoc   Drawn By:
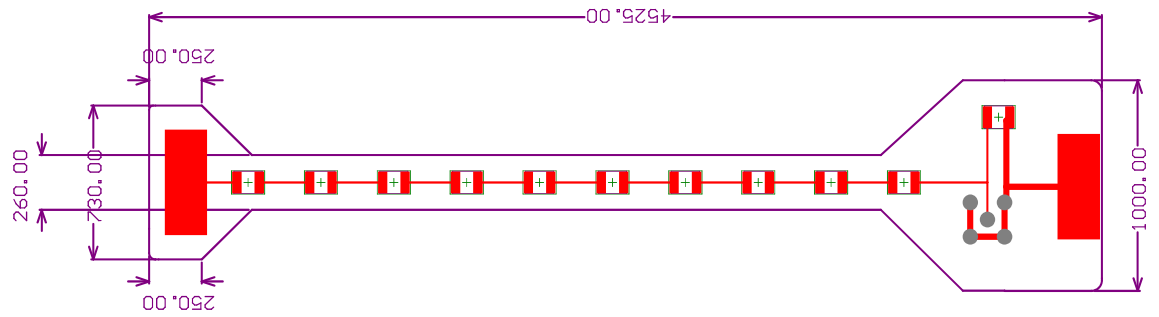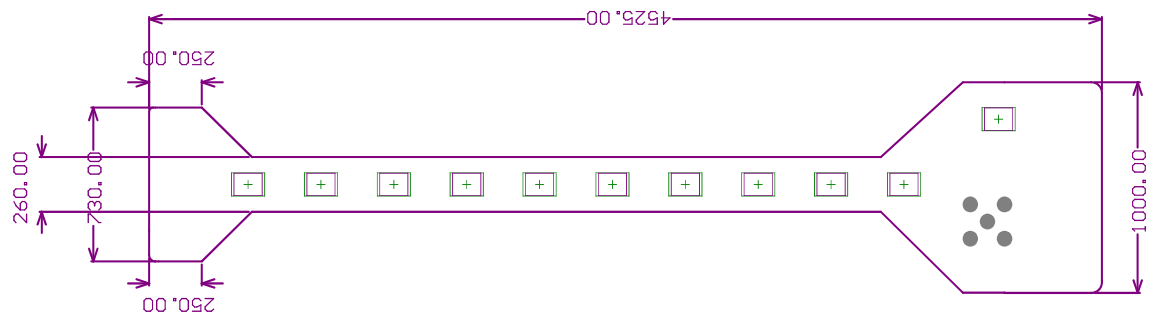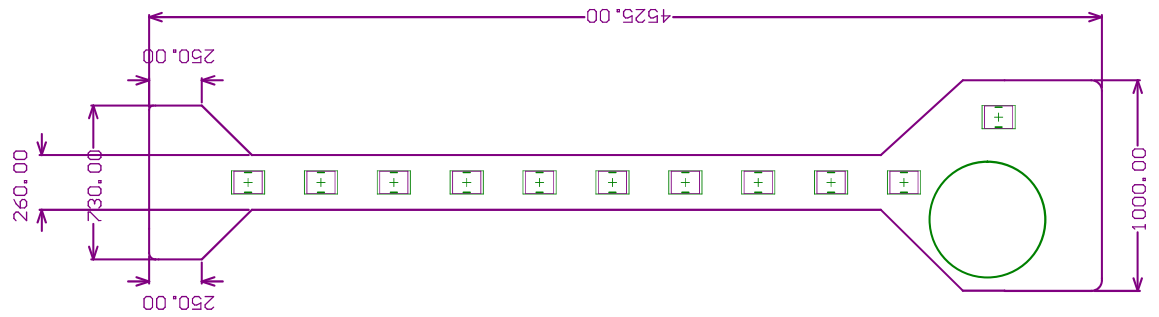
Appendix E

Voltage Doubler PCB

The PCB mount connectors are Rosenberger PN 51K201-400N5 right angle 50 Ω BNC jack connectors. The PCB is a standard 1.6 mm thick 2 layer PCB.
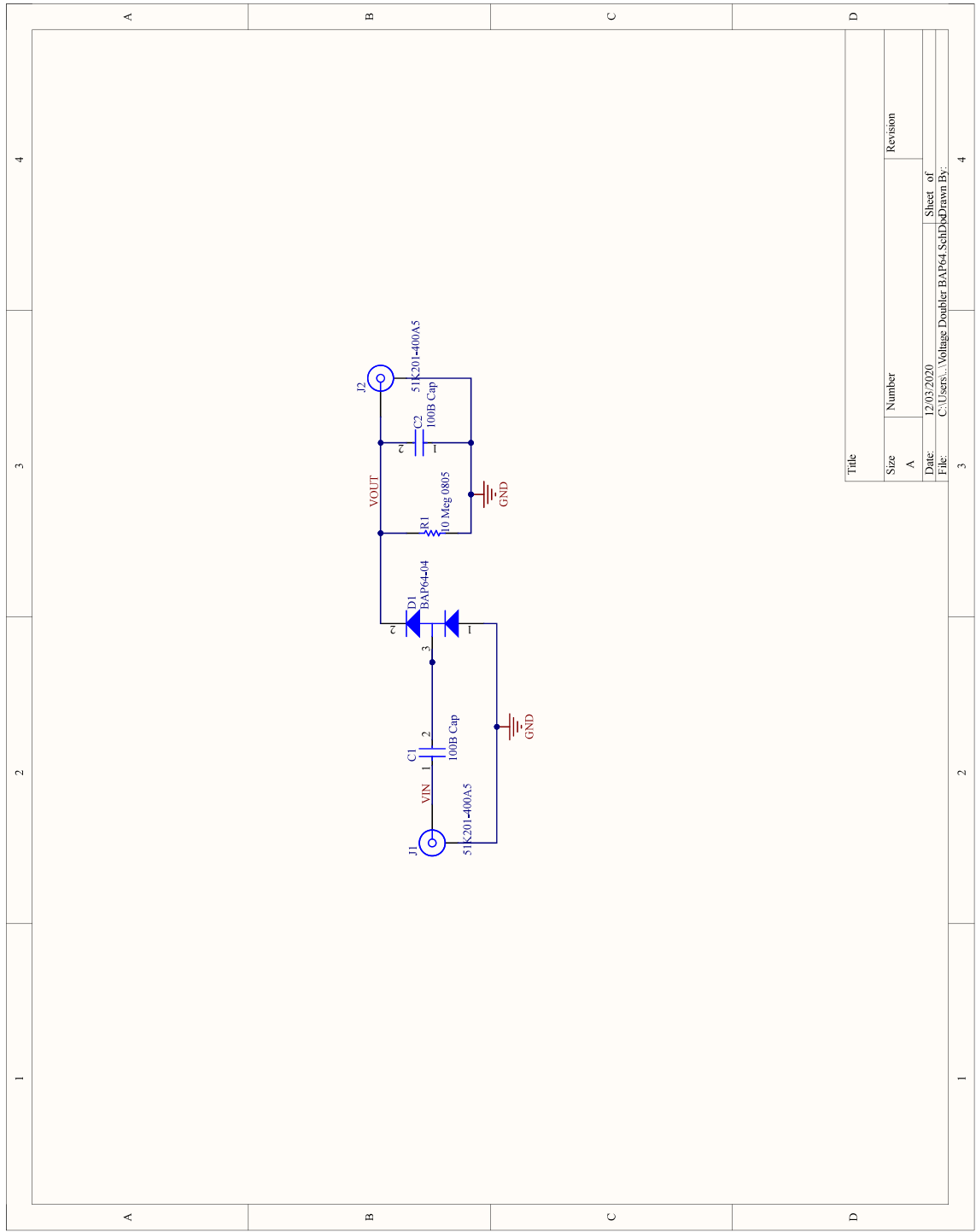
2.20 (in)

0.54 (in)

2.20 (in)

0.54 (in)

OUT
R1
D1 C2
C1 IN

2.20 (in)

0.54 (in)

RF Inductor project
PyPet Notrage Doubler
pog Baylass III

2.20 (in)

0.54 (in)
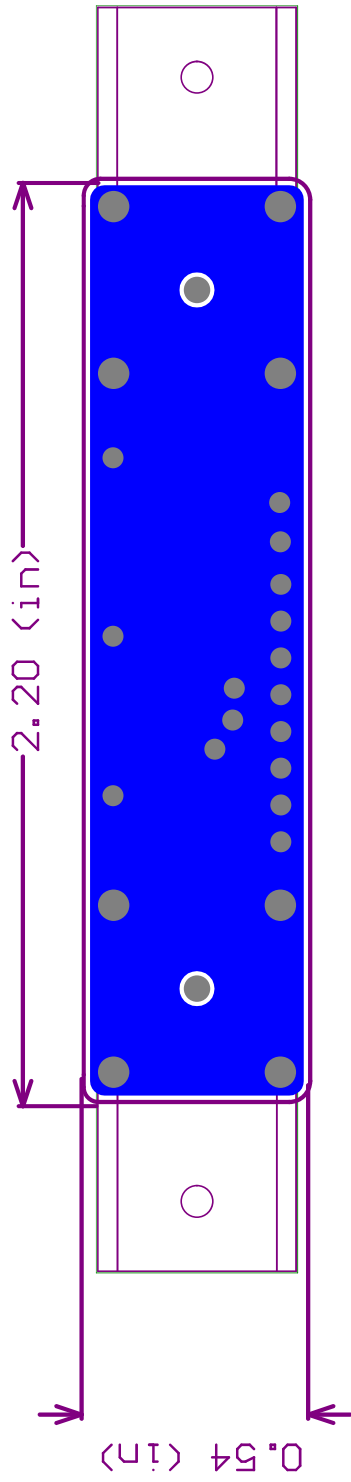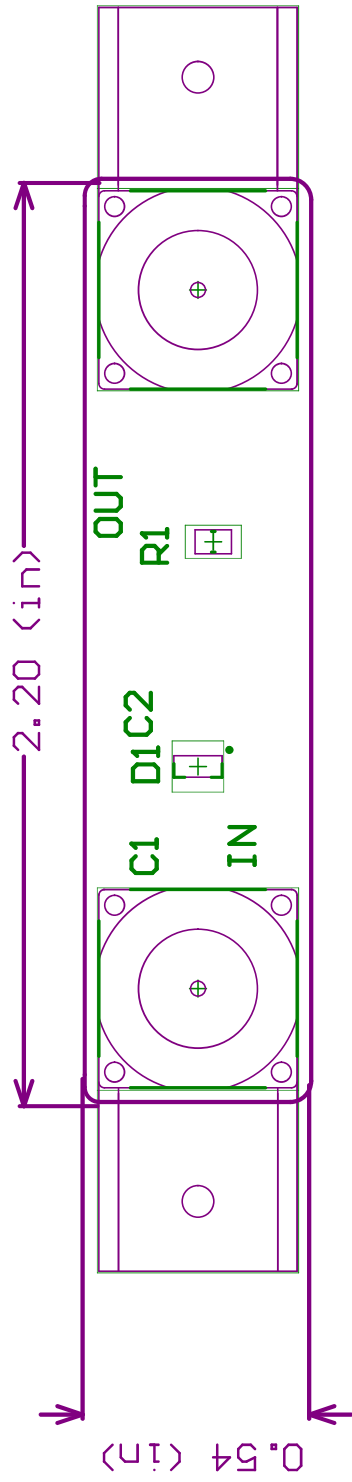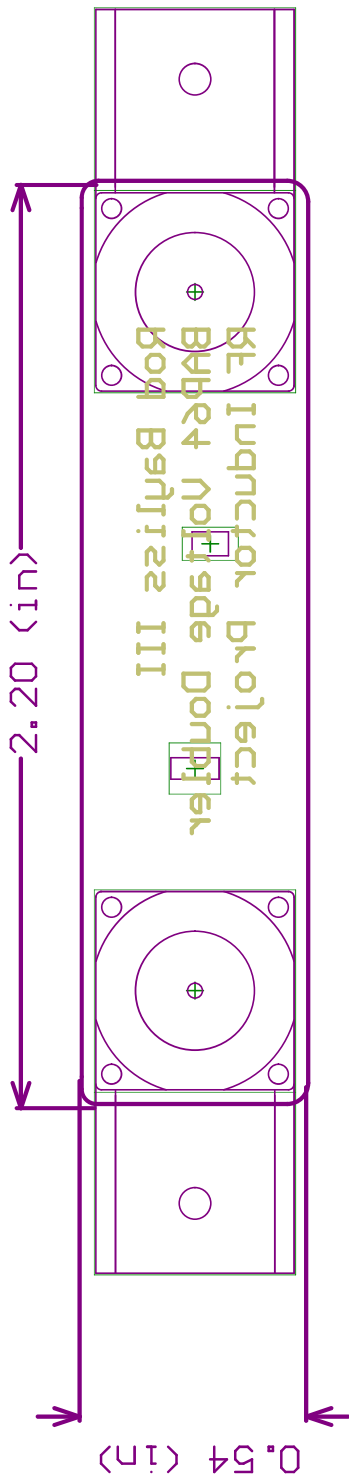
Appendix F

Ferrite Discs CAD Drawings
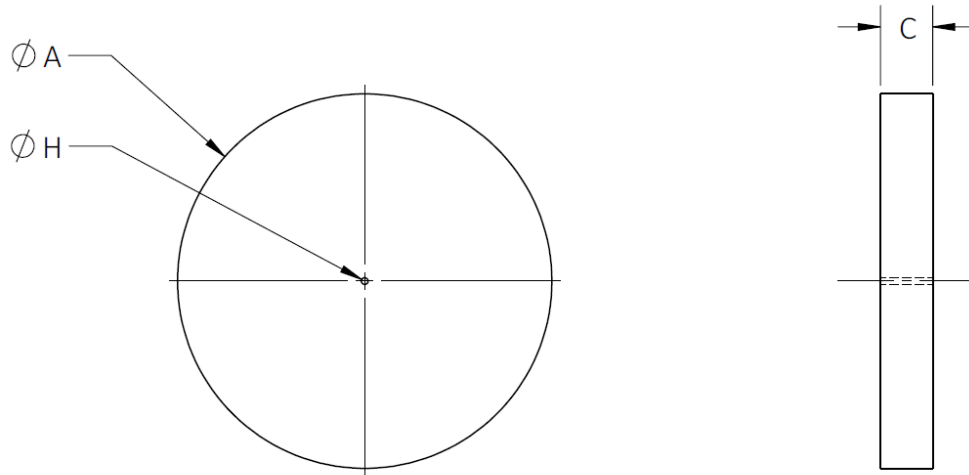
BOLD DIMENSIONS ARE IN MILLIMETERS, LIGHT DIMENSIONS ARE IN INCHES***

A (DVC)	C (1M)	H (PG)
112.000	**15.632**	**2.000**
4.3695 / 4.4495	0.6135 / 0.6175	0.0758 / 0.0818
4.4095 ± 0.0400	0.6155 ± 0.0020	0.0788 ± 0.0030

PROJECTED PRODUCTION CAPABILITY

A (DVC)	C (1M)	H (PG)
112.000	**15.632**	**2.000**
4.3215 / 4.4975	0.6105 / 0.6205	0.0758 / 0.0818
4.4095 ± 0.0880	0.6155 ± 0.0050	0.0788 ± 0.0030

Figure F-1: CAD Drawing of Ferrite End Cap. Two pieces are stacked to create a complete end cap.
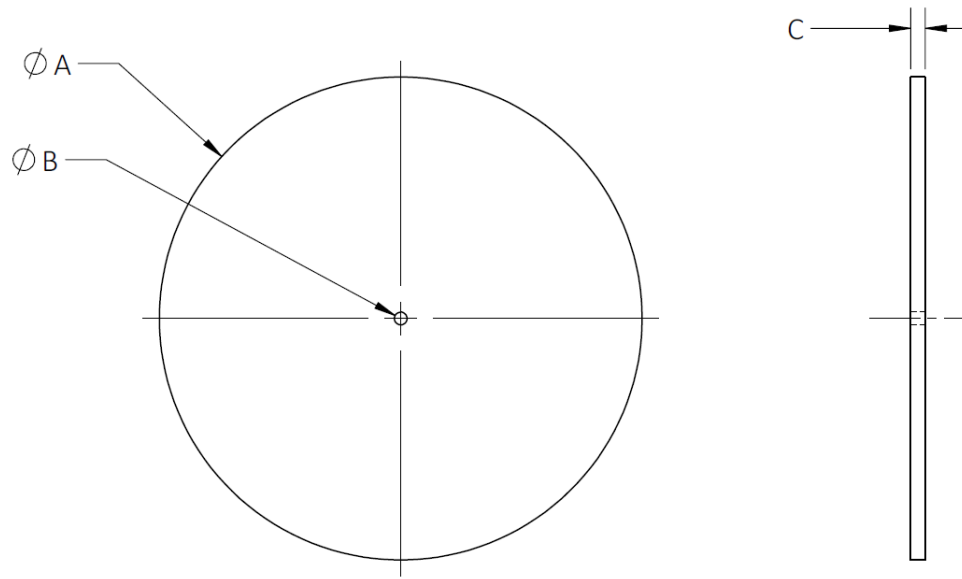
BOLD DIMENSIONS ARE IN MILLIMETERS, LIGHT DIMENSIONS ARE IN INCHES***

A (DVC)	C (1M)	H (PG)
75.526	**2.275**	**2.000**
2.9435 / 3.0035	0.0886 / 0.0906	0.0758 / 0.0818
2.973 ± 0.0300	0.0896 ± 0.0010	0.0788 ± 0.0030

PROJECTED PRODUCTION CAPABILITY

A (DVC)	C (1M)	H (PG)
75.526	**2.275**	**2.000**
2.9135 / 3.0335	0.0876 / 0.0916	0.0758 / 0.0818
2.973 ± 0.0600	0.0896 ± 0.0020	0.0788 ± 0.0030

Figure F-2: CAD Drawing of Ferrite Center Disc.

Appendix G

Capacitor Plates CAD Drawings

M4 x 0.7 mm thread, 8mm long, brass screws were used to affix the capacitor plates to the vacuum capacitor. The plates were manufactured from 0.25" thick super-conductive 101 copper sheet (McMaster-Carr).
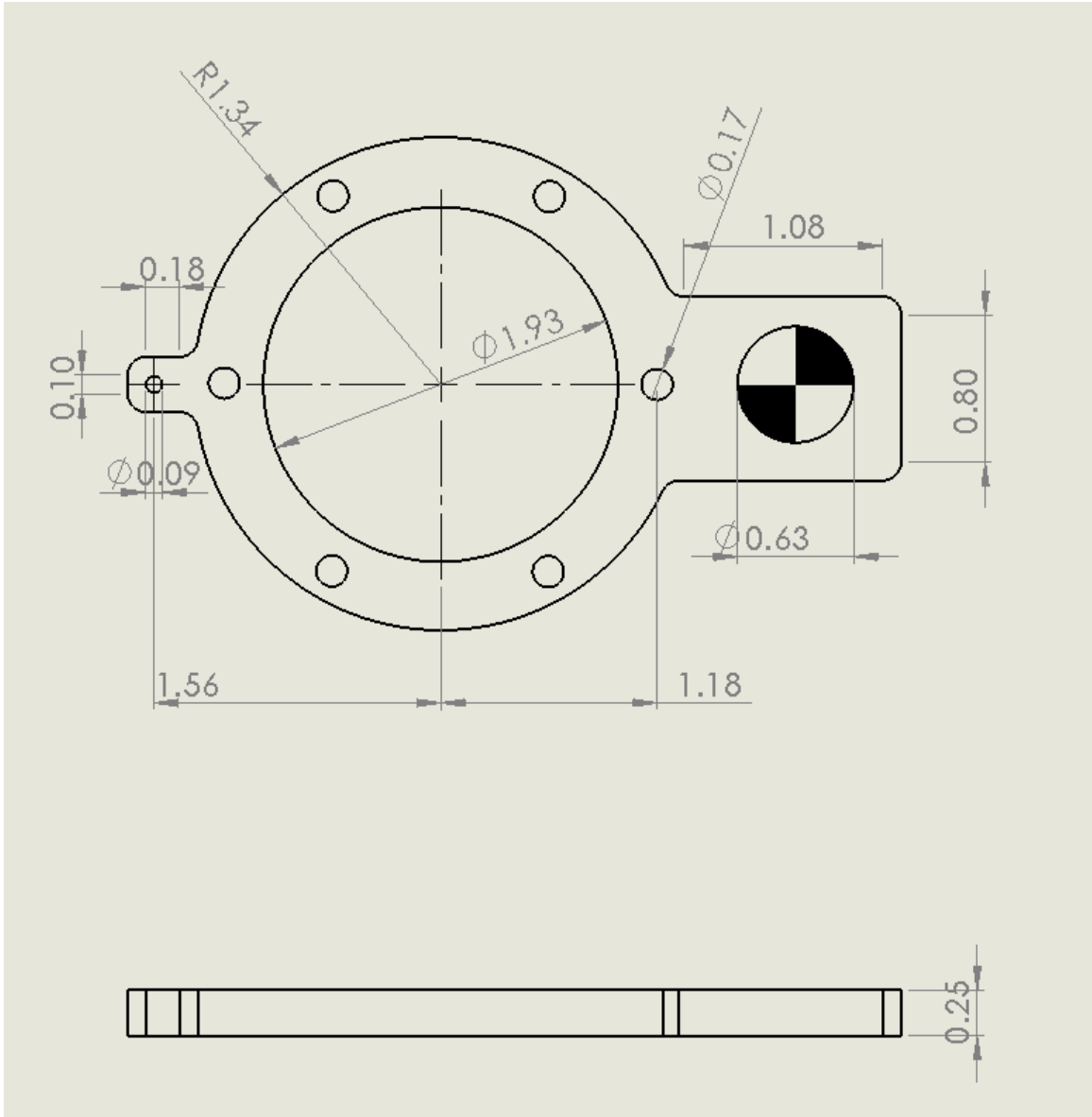
Figure G-1: CAD Drawing of Top Capacitor Plate.
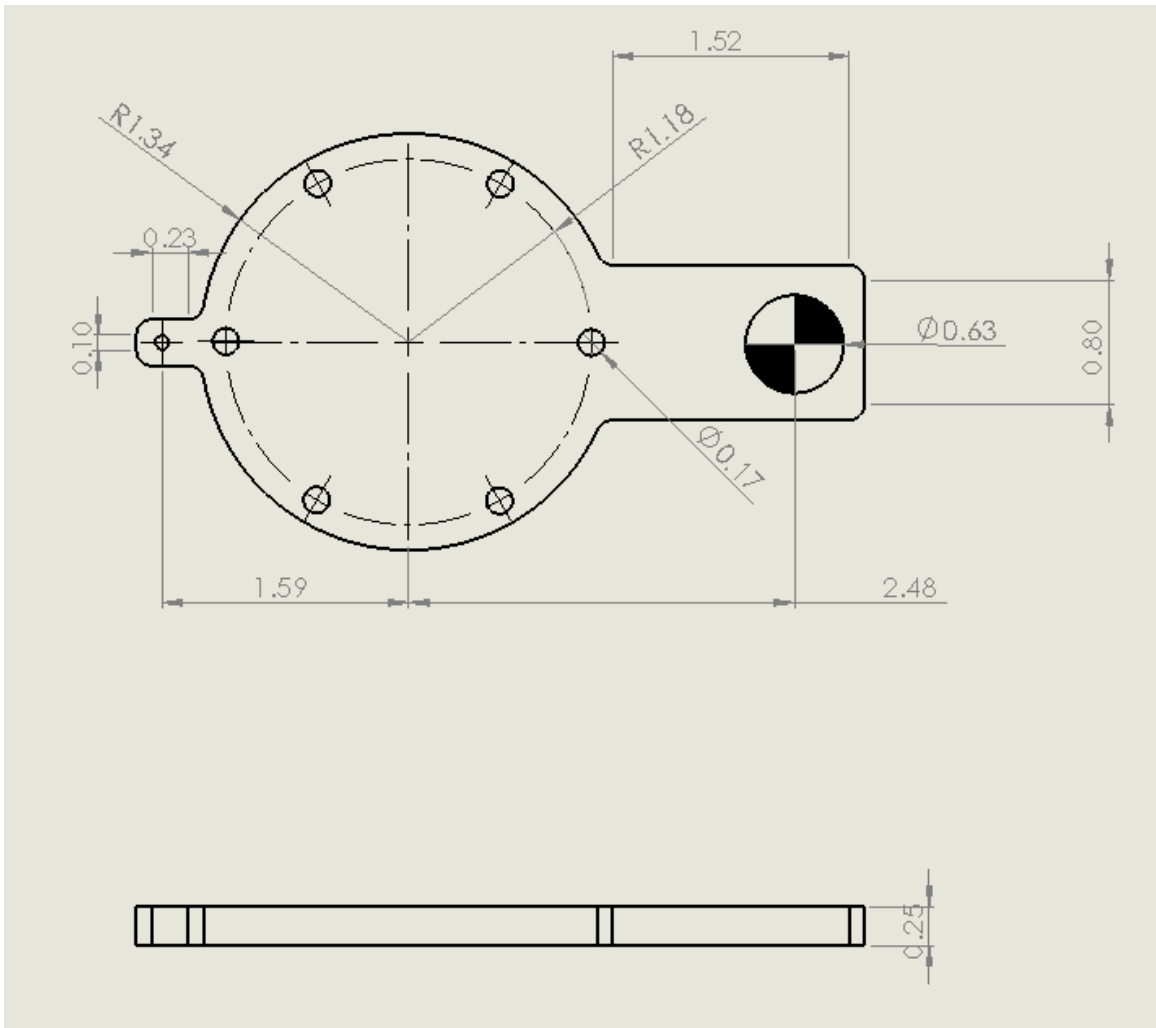
Figure G-2: CAD Drawing of Bottom Capacitor Plate.

Bibliography

[1] ANSYS Maxwell: Low Frequency Electromagnetic Field Simulation. Library Catalog: www.ansys.com.

[2] RF probe, August 2020. https://en.wikipedia.org/wiki/RF_probe.

[3] Anas Al Bastami, Alexander Jurkov, David Otten, Duy T. Nguyen, Aaron Radomski, and David J. Perreault. A 1.5 kW Radio-Frequency Tunable Matching Network Based on Phase-Switched Impedance Modulation. *IEEE Open Journal of Power Electronics*, 1:124–138, 2020.

[4] Yehui Han, Grace Cheung, An Li, Charles R. Sullivan, and David J. Perreault. Evaluation of Magnetic Materials for Very High Frequency Power Applications. *IEEE Transactions on Power Electronics*, 27(1):425–435, January 2012.

[5] Yehui Han and David J. Perreault. Inductor Design Methods With Low-Permeability RF Core Materials. *IEEE Transactions on Industry Applications*, 48(5):1616–1627, September 2012.

[6] Alex J. Hanson, Julia A. Belk, Seungbum Lim, Charles R. Sullivan, and David J. Perreault. Measurements and Performance Factor Comparisons of Magnetic Materials at High Frequency. *IEEE Transactions on Power Electronics*, 31(11):7909–7925, November 2016.

[7] Jiankun Hu and C.R. Sullivan. The quasi-distributed gap technique for planar inductors: design guidelines. In *IAS '97. Conference Record of the 1997 IEEE Industry Applications Conference Thirty-Second IAS Annual Meeting*, volume 2, pages 1147–1152 vol.2, October 1997. ISSN: 0197-2618.

[8] William Gerard Hurley, Tim Merkin, and Maeve Duffy. The Performance Factor for Magnetic Materials Revisited: The Effect of Core Losses on the Selection of Core Size in Transformers. *IEEE Power Electronics Magazine*, 5(3):26–34, September 2018.

[9] J.G. Kassakian, D.J. Perreault, M.F. Schlecht, and G.C. Verghese. Introduction to Magnetics Design. In *Principles of Power Electronics*. Cambridge University Press (to appear).

[10] E R Laithwaite. Magnetic equivalent circuits for electrical machines. *Proceedings of the IEE*, 114(11):1805–1809, November 1967.

[11] S.A. Mulder. Loss formulas for power ferrites and their use in transformer design. pages 1–16. Phillips Components, 1994.

[12] Charles R. Sullivan, Bradley A. Reese, Aaron L. F. Stein, and Phyo Aung Kyaw. On size and magnetics: Why small efficient power inductors are rare. In *2016 International Symposium on 3D Power Electronics Integration and Manufacturing (3D-PEIM)*, pages 1–23, June 2016.

[13] T. H. Lee. Passive Components. In *Planar Microwave Engineering: A Practical Guide to Theory, Measurement, and Circuits*, pages 140–142. Cambridge University Press, 1st edition, 2004.

[14] Rachel S. Yang, Alex J. Hanson, Bradley A. Reese, Charles R. Sullivan, and David J. Perreault. A Low-Loss Inductor Structure and Design Guidelines for High-Frequency Applications. *IEEE Transactions on Power Electronics*, 34(10):9993–10005, October 2019.

[15] Rachel S. Yang, Alex J. Hanson, Charles R. Sullivan, and David J. Perreault. Application Flexibility of a Low-Loss High-Frequency Inductor Structure. In *2020 IEEE Applied Power Electronics Conference and Exposition (APEC)*, pages 168–175, March 2020.